Simultaneous Estimation of Microphysical Parameters and Atmospheric State with Simulated Radar Data and Ensemble Square-root Kalman Filter. Part II: Parameter Estimation Experiments

Mingjing Tong and Ming Xue

Center for Analysis and Prediction of Storms and School of Meteorology
University of Oklahoma, Norman OK 73072

June, 2006

Submitted to Monthly Weather Review
Revised May, August 2007

Corresponding author address:
Ming Xue
Center for Analysis and Prediction of Storms,
National Weather Center, Suite 2500,
120 David L. Boren Blvd, Norman, OK 73072
mxue@ou.edu

Abstract

The ensemble Kalman filter method is applied to correct errors in five fundamental microphysical parameters that are closely involved in the definition of drop/particle size distributions of microphysical species in a commonly used single-moment ice microphysics scheme, for a model-simulated supercell storm, using radar data. The five parameters include the intercept parameters for rain, snow and hail/graupel, and the bulk densities of hail/graupel and snow. The ensemble square-root Kalman filter (EnSRF) is employed for simultaneous state and parameter estimation.

The five microphysical parameters are estimated individually or in different combinations starting from different initial guesses. A data selection procedure based on correlation information is introduced, which, combined with variance inflation, effectively avoids the collapse of the spread of parameter ensemble hence filter divergence. Our parameter estimation results demonstrate, for the first time, that the ensemble-based method can be used to correct model errors in microphysical parameters through simultaneous state and parameter estimation, using radar reflectivity observations. When error exists in only one of the microphysical parameters, the parameter can be successfully estimated without exception. The estimation of multiple parameters is less reliable, mainly because the identifiability of the parameters becomes weaker and the problem might have no unique solutions. The parameter estimation results are found to be very sensitive to the realization of the initial parameter ensemble, which is mainly related to the use of relatively small ensemble sizes. Increasing ensemble size generally improves the parameter estimation. The quality of parameter estimation also depends on the quality of observation data. It is also found that the results of state estimation are generally improved when simultaneous parameter estimation is performed, even when the estimated parameter values are not very accurate.

1. Introduction

Various studies over the recent years have demonstrated that the ensemble Kalman filter (EnKF) method (Evensen 1994; Burgers et al. 1998; Houtekamer and Mitchell 1998; Evensen 2003) and its variations (Anderson 2001; Bishop et al. 2001; Whitaker and Hamill 2002) form a viable approach to atmospheric data assimilation, for both large-scale (Houtekamer and Mitchell 2001; Houtekamer et al. 2005) and small-scale (Snyder and Zhang 2003; Dowell et al. 2004; Zhang et al. 2004; Tong and Xue 2005a; Xue et al. 2006) applications. For the convective-scale radar data assimilation, the flow-dependent multivariate background error covariances provided by the ensemble-based assimilation method play an essential role, because most state variables are not directly observed at the convective scale. It has been shown that dynamically consistent wind, thermodynamic and microphysical fields can be retrieved accurately using EnKF methods from simulated radar radial velocity and reflectivity observations (Snyder and Zhang 2003; Zhang et al. 2004; Tong and Xue 2005a; Xue et al. 2006). Encouraged by these Observing System Simulation Experiment (OSSE) results, researchers have been moving towards using real data (e.g. Dowell et al. 2004; Houtekamer et al. 2005; Tong 2006) and exploring the possibility of operational implementation of ensemble-based data assimilation methods (e.g. Houtekamer et al. 2005).

In most OSSE studies, only forecast errors due to uncertain initial conditions are taken into account, while forecast errors due to model deficiencies are neglected. However, in real-world applications, significant challenge can be encountered due to the presence of model error. With the EnKF, the flow-dependent multivariate covariances are estimated and evolved through the model evolution of each ensemble member. Whether they can be determined correctly depends on whether the model evolutions are correct and systematic model errors can cause the

ensemble member not being drawn from the distribution that produces truth because the model attractor and the system attractor differ (Hansen 2002).

Systematic errors can result from uncertain parameters used in the prediction model. One way to account for the model error of this type is through parameter estimation, so that the parameters can be more adequately constrained by available observations. Different techniques, such as the maximum likelihood method (Dee 1995), extended Kalman filter (Hao and Ghil 1995) and variational method (Yu and O'Brien 1991; Zou et al. 1992), have been applied to the parameter estimation problem in meteorology and oceanography. Recently, Crook et al. (2004) applied the 4DVAR method to estimate a coefficient in a hydrometeor terminal velocity formulation of their cloud model.

Anderson (2001) first suggested that the EnKF can be used for parameter estimation by including the model parameters as part of the model state and estimating them simultaneously with the model state. Annan et al. (2005b) successfully applied the EnKF method to simultaneously estimate 12 parameters in a low-resolution coupled atmosphere-ocean model with steady-state dynamics. Annan and Hargreavers (2004) also successfully applied this method to perform multivariate parameter estimation in the presence of chaotic dynamics with the Lorenz model. More recently, they extended their results to a realistic intermediate complexity atmospheric GCM with identical twin experiments and reanalysis data (Annan et al. 2005a). However, in contrast to weather prediction, the climate forecasts depend strongly on parameterizations rather than initial conditions. Kivman (2003) found that the EnKF performed poorly when applied to simultaneous state and parameter estimation in the Lorenz model. He attributed this to utilizing only two statistical moments in the analysis step by all Kalman filter-based methods, which are unable to deal with highly non-Gaussian probability distributions in

the parameter space. Experiments assimilating simulated surface observations into a parameterized 1D PBL model as well as estimating the parameter of soil moisture availability by Hacker and Snyder (2005) suggested that the EnKF may help mitigate model error via parameter estimation. Aksoy *et al.* (2006b) applied the EnKF method to simultaneous estimation of up to 6 parameters and the model state with a two-dimensional, hydrostatic, non-rotating, and incompressible sea-breeze model. They found that the estimation of single imperfect parameters with the EnKF is successful, while the quality of estimation deteriorates when the number of estimated parameters increases.

Errors in microphysical parameterization have direct impact on simulation (e.g. Gilmore et al. 2004) and data assimilation (e.g. Crook et al. 2004) for convective systems. The basic assumption for the bulk microphysics scheme is that the particle or drop size distributions (DSDs) can be represented in functional forms. For single-moment bulk microphysics scheme, a large part of the error lies with the uncertain values assigned to the parameters that are used to define the drop size distributions, which are usually predetermined constants. In reality, those parameters can vary with space and time and among systems in different large environment. The purpose of this two-part study is to examine the impact of the errors in these microphysical parameters on the retrieved model state and to correct these errors, when possible, using the EnKF method through parameter estimation. To our knowledge, this is the first attempt as such.

The microphysics scheme used in the ARPS model (Xue et al. 2000; Xue et al. 2001; Xue et al. 2003), on which our EnKF data assimilation system is based, is the 5-class (cloud water, rain, cloud ice, snow and hail/graupel) single-moment bulk scheme after Lin et al. (1983, LFO83 hereafter). Additional information of the microphysics scheme can be found in Part I of this study (Tong and Xue 2007, Part I hereafter). The microphysical parameters to be estimated

include the intercept parameters of hail, snow and rain drop size distributions, the densities of hail and snow. The sensitivity of the model forecast within data assimilation cycles for a simulated supercell thunderstorm to these parameters are analyzed in detail in Part I, together with discussions on issues associated with parameter identifiability. In this second part, we focus on estimating those microphysical parameters using the EnKF method and radar data.

The remainder of this paper is organized as follows. In section 2, we describe our parameter estimation procedures. The results of parameter estimation experiments, based on simulated data for a supercell storm, are discussed in section 3. Parameter identifiability is further discussed in section 4. Summary and conclusions are given in section 5.

2. The design of parameter estimation experiments

a. General configuration

As the first attempt to estimate uncertain microphysical parameters, OSSEs are conducted. The information of the prediction model and the truth simulation can be found in Part I. In short, the ARPS (Xue et al. 2000; Xue et al. 2001; Xue et al. 2003) model is used in a 3D cloud model mode and the prognostic variables include three velocity components, potential temperature, pressure, and six categories of water substances: water vapor specific humidity, and mixing ratios for cloud water, q_c; rainwater, q_r; cloud ice, q_i; snow, q_s; and hail, q_h. These prognostic variables are the state variables to be estimated. We do not update the turbulent kinetic energy which is also predicted by the model. The truth simulation is for the May 20, 1977 Del City, Oklahoma supercell storm case (Ray et al. 1981; Xue et al. 2001). The horizontal and vertical grid spacings are 2 km and 500 m, respectively, in both truth simulation and assimilation experiments. The model grid is 64 × 64 × 16 km, and the radar is located at the southwest corner of the grid.

The ensemble square root filter (EnSRF, Whitaker and Hamill 2002) is used for state and parameter estimation. The EnSRF data assimilation configurations as well as the observation operators are described in Part I. Briefly, The initial ensemble was generated by adding spatially smoothed perturbations to the first guess of the initial condition that is horizontally homogeneous as defined by the May 20, 1977 Del City, Oklahoma supercell sounding. The first ensemble forecast cycle starts at 20 minutes of the simulated supercell storm. Radar volume data are assimilated every 5 minutes. Both radial velocity and reflectivity, including reflectivity in non-precipitation regions, are used for state estimation while reflectivity data only are used for parameter estimation. Forty or one hundred ensemble members are used in the experiments to be reported in this paper.

As mentioned earlier, the parameter estimation with the EnSRF is realized by considering the parameters as part of the model state, an approach that is often referred to as the state vector augmentation. In the single-moment bulk microphysics scheme of LFO83 used by the ARPS, the DSD parameters are spatially and temporally invariant. We will first estimate the five DSD parameters individually, and then increase the number of simultaneously estimated parameters gradually from two to five. The parameters that are not estimated assume their true values.

Suppose vector $\mathbf{p} = \left(p_1, ..., p_L \right)^{\mathrm{T}}$ is the L-dimensional vector of the unknown DSD parameters that are to be estimated, where L varies from 1 to 5 in our study. The prior information on the unknown DSD parameters is their range of variations. The admissible set of $\mathbf{p}$ based on parameter range ($P_{ad} = \left\{ \mathbf{p} \mid \underline{p}_i \le p_i \le \overline{p}_i, i = 1, 2, ..., L \right\}^{\mathrm{T}}$) has been discussed and given in Part I. To investigate the uniqueness of the inverse problem that is intimately related to parameter identifiability, our parameter estimation experiments start from different initial guesses of $\mathbf{p}$, which are chosen from P_{ad}. An initial parameter ensemble is constructed by

randomly sampling the parameters from their prior distributions. The uncertainty associated with the intercept parameters can be more than an order of magnitude (see Part I). Initial sampling of the parameter ensemble from a broad prior distribution can easily result in unphysical negative values. Problems in the analysis can also result in negative intercept parameter and density. Therefore, the five microphysical parameters are logarithmically transformed and multiplied by 10. The use of the logarithmic form may also improve the Gaussian assumption on the parameter error distribution. Table 1 lists the true values of the logarithmically transformed parameters and their upper and lower bounds. Working with the new parameter vector $\mathbf{P} = 10\log_{10}(\mathbf{p}) = (P_1, ..., P_L)^{\mathrm{T}}$, the initial ensemble of P_i is randomly drawn from $N(P_{i0}, \sigma_{P_i}^2)$, where P_{i0} is an initial guess of P_i. Ideally, the initial ensemble spread of parameter P_i, i.e., the standard deviation, σ_{P_i}, of the prior distribution of the parameter, should represent the error in the first guess, P_{i0}. However, the initial error is usually unknown in reality. In this study, the ensemble spread of each DSD parameter is initialized to be roughly half of its largest admissible deviation from its default values in the model, i.e., $\sigma_{P_i} = 0.5\max(|\underline{P}_i - P_i^t|, |\overline{P}_i - P_i^t|)$ (see Table 1), for all parameter estimation experiments.

The first requirement of parameter identifiability is that all estimations must converge to the same point $\mathbf{P}^t$ regardless of the starting point $\mathbf{P}_0$ (Sun et al. 2001). Therefore, different initial guesses are tested for the estimation of each parameter vector $\mathbf{P}$. However, numerical experiments can only be conducted with limited number of starting points $\mathbf{P}_0$. The conclusions taken from the limited number of numerical trials should be more robust, if the randomness in the filter configuration is taken into account. The randomness comes from the realization of the initial ensemble for parameters as well as model state variables and the realization of the observation errors. In this study, different realizations of the initial ensemble are applied to the

experiments estimating the same parameter vector **P** with different initial guesses $\mathbf{P}_0$. The radar observation data used in different experiments estimating the same **P** are also generated with different realizations of observation errors.

In our EnSRF system, at each analysis time, the covariances between the parameters and the observations are calculated and used to update the parameters. Our sensitivity analysis in Part I showed that the forecast radar reflectivity is more sensitive to the microphysical parameters than radial velocity. The reflectivity also has a higher correlation with each of the microphysical parameters than radial velocity. Our initial test using radial velocity data alone for parameter estimation was not successful. As a result, only reflectivity data greater than 10 dBZ will be considered for parameter estimation.

b. Data selection procedure

A critical problem we were confronted with during the parameter estimation is 'filter divergence'. The tendency of filter divergence is much more pronounced with the estimation of global parameters than with model state because of two reasons. First, at each analysis step, about 400 (in the first cycle) to more than 4000 (in the last cycle) reflectivity data are available for updating the few global parameters, while the data used to update model variables at certain grid point are limited through spatial covariance localization. The parameter ensemble spread narrows quickly by the repeated application of the data. Another reason for such continuous narrowing is that these parameters are not dynamic; their errors do not grow during the forecast as those of state variables do. In our case, without a special treatment that prevents 'filter divergence', the parameter ensemble becomes useless after only two or three assimilation cycles and the parameters can no longer be influenced by observations before they converge to their true values.

To compensate for the infinitely diminishing of the parameter ensemble, a similar ensemble inflation procedure as used in Aksoy *et al.* (2006b) is employed. A minimum standard deviation $\underline{\sigma}_{P_i}$ is pre-specified, so that when the prior standard deviation becomes smaller than $\underline{\sigma}_{P_i}$, the parameter ensemble spread is adjusted back to $\underline{\sigma}_{P_i}$. For successful parameter estimation, the error in the ensemble-mean should have negligible impact on the state estimation. We found that the model state estimations are not sensitive to the errors in the parameters, if the absolute error of the logarithmically transformed intercept parameters is no larger than 1 and that of the bulk densities is no larger than 0.5. These values will be used as the minimum ensemble spreads $\underline{\sigma}_{P_i}$ for parameter ensemble inflation.

However, our early single-parameter estimation experiments show that if all reflectivity data larger than 10 dBZ are used, the minimum ensemble spread $\underline{\sigma}_{P_i}$ has to be much smaller than that given in Table 1; otherwise, the estimated parameter is over adjusted, which is manifested as large oscillations in the estimated parameter time series around the true value (Tong and Xue 2005b). The over-adjustment to the estimated parameter is again caused by the large number of data used for parameter estimation. In the estimation system, the correlation information determines the direction to which the parameter should be adjusted, while the variance determines the amount of adjustment. As shown in Part I, the reflectivity in a large part of the storm is highly correlated with the individual parameters, which implies that a major portion of the data could provide the right direction of adjustment, but constantly inflating the variance after each parameter adjustment can cause over-adjustment.

In Part I, we also found that the correlations between the DSD parameters and the reflectivity decrease as the number of uncertain parameters increases. In many regions of the storm, the correlations become very weak ($|r| < 0.2$) for some parameters. This may explain why

the results of our early multiple-parameter estimation experiments, in which all reflectivity data are used to correct the values of the parameters, are poor, because the data in weak correlation regions cannot provide reliable direction information. Since not all reflectivity data within the storm are effective in correcting the errors in the parameters, in this study we introduce a new data selection procedure based on prior correlation information.

At each analysis time, we first calculate the correlation between each estimated parameter and the reflectivity at all data points from ensemble members. We then sort the correlations and pick the data points with larger correlations for the corresponding parameter. We fix the minimum ensemble spread at the upper bound of the ensemble mean error of the estimated parameter, $\underline{\sigma}_{P_i}$, that would have a negligible impact on the state estimation (Table 1). The number of data to be used for parameter estimation is adjustable. We tested the number of data from 20 to 60 based on single-parameter experiments and decided on 30. A smaller number of data leads to a slower convergence rate in some experiments, and a number larger than 50 results in over-adjustment to some parameters. There is no significant difference between experiments using 30 and 40 data.

3. Results and discussions

a. Results of experiments estimating single parameters

All single-parameter estimation experiments reported here use 40 ensemble members. The results of estimating the five microphysical parameters individually (with the other four having their true value) are presented in Fig. 1. For each parameter, results from three experiments are shown (in different columns of Fig. 1), with each starting from a different initial guess. These initial guesses are listed in Table 2. Fig. 1 shows the evolutions of the mean and

spread of the parameters during the 80 min assimilation period, from 20 to 100 min of model time. In each plot, the thick solid step-like curve represents the ensemble mean while the thin dashed lines indicate one-standard-deviation (1-σ_{P_i}) ensemble width. The values at 20 min indicate the initial parameter distributions. The true parameter values are shown by the thick straight horizontal lines. The experiments shown in Fig. 1 also have different random realizations of the initial ensemble and observation errors, for reasons discussed in section 2.

It can be seen from Fig. 1 that within a few (usually 4 to 5) assimilation cycles, the posterior ensemble spread of the estimated parameter decreases to the pre-specified minimum ensemble spread, $\underline{\sigma}_{P_i}$. The scenario of a successful parameter estimation should be that the absolute error of the estimated parameter is smaller than or very close to $\underline{\sigma}_{P_i}$. In the former case, the true value of the estimated parameter is located within the 1-$\underline{\sigma}_{P_i}$ ensemble width. This is because that $\underline{\sigma}_{P_i}$ is assigned to be the upper bound of the error that would have a negligible effect on the model state estimation. Generally, the results show that all five parameters can converge to their true values in these single-parameter experiments, albeit at different rates. The estimations of ρ_h appear most effective (Fig. 1m, n, o); the estimated ρ_h converges to the true value after only 5 assimilation cycles. After that, its error remains no greater than $\underline{\sigma}_{P_i}$.

The estimation of n_{0h} is also very good. After approaching the true value after the first 3-5 cycles, the estimated n_{0h} remains very close to the true value most of the time (Fig. 1a, b, c). In some experiments, the estimated parameter oscillates around the true value, sometimes outside the range of one $\underline{\sigma}_P$ (e.g., the estimation of n_{0s} in Fig. 1f). In other cases, temporary deviation from the true value occurs after the parameter has approached the true value (e.g., Fig. 1h, i, k).

In Part I, we found that the model forecast in terms of reflectivity has a larger sensitivity

to ρ_h and n_{0h}. The minima of the response functions for the two parameters are located very close to their true values (Fig. 3 in Part I). The model also responds to changes in these two parameters faster than to other parameters. However, we will see later that there are additional factors that can affect the behaviors of the estimated parameters.

The experiments in Fig. 1 show that the estimated parameter does not always consistently approach the truth from the beginning. In the first 1 or 2 assimilation cycles, the parameter can deviate further away from the truth. This has happened to all five parameters (e.g. Fig. 1a, e, h, l, m). Such initial deviations can generally be corrected within the next 1 to 2 cycles (e.g. Fig. 1a, m). However, in some cases, the deviation can significantly affect the convergence rate of parameter estimation. For example, the ensemble means of n_{0s} in Fig. 1d and ρ_s in Fig. 1l reach beyond their admissible values within the first 2 assimilation cycles; it takes several assimilation cycles to draw them back to their reasonable and eventually true values. This significantly slows down the parameter estimation processes.

At least two factors can affect the convergence rate of parameter estimation. One is with the magnitude, speed and accuracy of the estimated model response to the parameter error during the data assimilation process. Since our assimilations start from a very poor initial state, the forecast error tends to be dominated by the initial condition error during the early cycles, making the model response to the parameter errors hard to identify. The parameter estimation improves as the state estimation improves in later cycles.

Another factor is associated with the random sampling of the initial parameter perturbations. Fig. 2 shows the effect of the randomness in drawing the initial parameter ensemble from a specific distribution on the results of parameter estimation. The estimation of n_{0h} and ρ_s with first guesses of 4×10^5 m^{-3} and 400 kg m^{-3}, respectively, are presented. For each

parameter, five estimation experiments were perform, with the only difference being with the realization of the initial parameter ensemble. It can be seen that different realizations result in different convergence rate of the estimated parameter. Even though sensitivity experiments N0h45 and ρ_s400 in Part I show that the system responds quicker to the corresponding change in n_{0h} than that in ρ_s, the quality of initial sampling can still cause slow convergence for n_{0h} (e.g., the thick gray curve in Fig. 2a). On the other hand, the estimated ρ_s can approach the truth within 3 assimilation cycles for some cases (e.g., the thick black curve in Fig. 2b). Clearly, the realization of the initial parameter ensemble can have a significant impact on the convergence rate.

The impact of parameter estimation on the model state is shown in Fig. 3. The results of experiments ρ_h400, N0r87, ρ_s400 (dashed curves), for which the initial guesses of ρ_h, n_{0r} and ρ_s are 400 kg m^{-3}, 8×10^7 m^{-4} and 400 kg m^{-3}, respectively, are presented. The corresponding parameter evolutions can be found in Fig. 1m, Fig. 1i and Fig. 1l. The results of another set of experiments (ρ_h400NE, N0r87NE and ρ_s400NE), in which the wrong initial guesses of the parameters are kept without parameter estimation, as well as the results of CNTL (the perfect-parameter case) are also shown in the figure for comparison purposes. Only the rms errors for the microphysical species are shown here because they are more directly affected by the microphysical parameter errors. The error curves for other variables present a similar picture.

For cases of very successful parameter estimation, such as experiment ρ_h400 in Fig. 1m, the errors in the estimated model variables are indistinguishable from those of CNTL (Fig. 3a-e). In the experiment estimating n_{0r} (N0r87), parameter estimation definitely improves the model state estimation over the case without parameter estimation (N0r87NE, Fig. 3f-j). The errors of the state variables are very close to those of CNTL most of the time, except for the larger errors

in q_r between 65 and 85 min, which is consistent with the larger error in the estimated n_{0r} during that time period (Fig. 1i). The third row of Fig. 3 shows the results of a relatively poor case of ρ_s estimation. With the parameter estimation, the errors in the model state variables are even larger than the case of no parameter estimation (ρ_s400NE) before 60 min. This is mainly due to the incorrect estimation of ρ_s within the first few assimilation cycles; the error in the estimated ρ_s is lager than its initial error before 50 min (Fig. 1l). However, as the estimated ρ_s converges to the true value, the errors in the state variables eventually become comparable to those of CNTL, in the last 3 to 4 cycles.

Although a limited number of trials are presented here for single-parameter estimation, in all cases that we have tried, the estimated parameter eventually converges to the true value regardless of the initial guess, as long as it is within the admissible bounds. This is supported by the findings in Part I that the response function for each of the microphysical parameter has a unique global minimum.

b. Results of multiple parameter estimation

In this subsection, we present the results of the experiments, in which multiple microphysical parameters in different combinations contain error and are estimated. The parameters not estimated are assumed perfect.

To investigate the uniqueness of the inverse solution for multiple-parameter estimation and to reduce the chance for the results to be fortuitous in some way, two values are picked from the admissible set P_{ad} for each parameter and the combinations of the chosen values are used as the initial guesses of the parameter vectors. The chosen initial values for each microphysical parameter are listed in Table 3.

1) Simultaneous estimation of two parameters

Fig. 4 shows the results of the experiments estimating (n_{0h}, ρ_h) using forty ensemble members. Four combinations of the initial guesses of these two parameters, namely, (4×10^5 m^{-4}, 400 kg m^{-3}), (4×10^5 m^{-4}, 700 kg m^{-3}), (4×10^6 m^{-4}, 400 kg m^{-3}) and (4×10^6 m^{-4}, 700 kg m^{-3}), are tested. These four initial guesses represent q_h distributions with the mass more heavily weighted toward small graupels than that represented by the true values of (4×10^4 m^{-4}, 913 kg m^{-3}). It can be seen from Fig. 4 that the estimated parameters converge to their truth values in all four cases, but generally at slower rates than those of corresponding parameters in the single parameter estimation experiments (c.f. Fig. 1).

Fig. 5a-e and Fig. 5f-j show, respectively, the rms errors of the estimated hydrometeor mixing ratios from the experiments shown in the 1st and 4th columns of Fig. 4. As can be seen, the errors in the two parameters, when remain uncorrected, lead to rather poor estimations of the hydrometeor species, especially for q_s and q_h (gray curves). Through parameter estimation, the analyses are significantly improved. In both experiments, after the two parameters converge to their true values, the mixing ratio rms errors become very close to those of CNTL.

The results of simultaneous estimation of two snow parameters, (n_{0s}, ρ_s), are shown in Fig. 6. The four initial guesses used for the two parameters are (3×10^7 m^{-4}, 300 kg m^{-3}), (3×10^7 m^{-4}, 50 kg m^{-3}), (7×10^5 m^{-4}, 300 kg m^{-3}) and (7×10^5 m^{-4}, 50 kg m^{-3}). We first performed experiments using 40 ensemble members, which are shown by the gray curves in the figure. It can be seen that the results are generally not very good. In the four cases, either the two parameters converge to the true values slowly (gray curves in the 1st and 3rd columns), or one or both parameters do not converge to the true values at all (gray curves in the 2nd and 4th columns). We repeated the four experiments using 100 ensemble members (black curves in Fig. 6). The large ensemble generally improved that estimation, as seen, e.g., from the 2nd and 4th columns of

Fig. 6. However, even with 100 members, the estimations of (n_{0s}, ρ_s) are still not as good as those of the (n_{0h}, ρ_h) estimation case (c.f., Fig. 4), in term of the convergence rate and estimation accuracy. Consistently, the model state estimations are not as good compared to Fig. 5, although improvement is still significant compared to the case of no parameter estimation (not shown).

2) Simultaneous estimation of three parameters

The results of simultaneously estimating three intercept parameters together are presented in Fig. 7. Based on the two initial guesses of each intercept parameter in Table 3, 8 combinations of initial guesses were used for estimating these three parameters. The experiments were first performed using 40 ensemble members, and the results are shown in the left column of Fig. 7. The different line types represent these 8 different experiments.

It can be seen from Fig. 7a, Fig. 7c and Fig. 7e that even with 40 ensemble members, the three intercept parameters can generally converge to the levels that are close to the true values. The estimation of n_{0h} and n_{0r} are better than that of n_{0s}, which has a larger variability among different cases. The estimated n_{0s} also approaches the true value slower than the other two parameters. As the estimation reaches to the end of the assimilation cycles, the absolute ensemble mean errors of all three parameters, averaged over the 8 experiment, (gray curves in Fig. 7b, Fig. 7d and Fig. 7f) decrease below 2 $\underline{\sigma}_{P_i}$.

We repeated the above eight experiments using 100 ensemble members. Fig. 7 shows that the large ensemble size (solid black curves in right column) significantly improves the estimation. The averaged errors of three intercept parameters decrease faster and to a lower level than in the 40 member case. The use of error free data further improves the parameter estimation results (black dashed curves in the right column of Fig. 7; more on this later).

3) Simultaneous estimation of four parameters

In this set of experiments, the hail density is added to the list of three intercept parameters A total of 16 combinations of the initial guesses of n_{0r}, n_{0s}, n_{0h}, and ρ_h were tested initially using 40 ensemble members. The average absolute ensemble mean parameter errors of the 16 experiments are shown by the gray curves in Fig. 8. Compared to the three–parameter case (gray curves in Fig. 7b, d, f), the simultaneous estimations of four parameters are much worse. This indicates increased difficulties when more parameters are uncertain.

To improve the estimation, the experiments are repeated with 100 ensemble members. Even more significant improvement is found than the three-parameter case. Fig. 8 shows that in this case, the averaged absolute error of n_{0r} (black curves in Fig. 8a) decreases below 2 $\underline{\sigma}_{P_i}$ after 5 assimilation cycles and is reduced below 1 $\underline{\sigma}_{P_i}$ in the last 3 assimilation cycles. At the end of the assimilation cycles, the errors of n_{0s}, n_{0h} and ρ_h are all between 1 $\underline{\sigma}_{P_i}$ and 2 $\underline{\sigma}_{P_i}$.

To illustrate the variations among the experiments with different initial guesses, the evolution of the parameter distributions of 6 of the 16 experiments using 100 ensemble members are shown in Fig. 9. In the two cases shown in the 1st column, all four parameters converge to their true values; the resultant errors of all four parameters are no larger than $\underline{\sigma}_{P_i}$. The two cases shown in the 2nd column of Fig. 9 represent some of the cases where the 4 parameters approach the true values but the ending errors for some of the parameters are around $2\underline{\sigma}_{P_i}$. In the two cases shown in the 3rd column, two or three parameters approach the true values slowly and some of them have errors larger than $3\underline{\sigma}_{P_i}$ at the end. The relatively poor estimation usually happens to n_{0h} and ρ_h, and sometimes to n_{0s}. The intercept parameter of rain is estimated accurately in all cases.

The impact of the four-parameter set on the state estimation is shown in Fig. 10, in which

the ensemble mean *rms* errors of the mixing ratios from the 3 experiments corresponding to the black curves in each column of Fig. 9 are presented. The *rms* errors from the experiment with successful parameter estimation (black curves in Fig. 9a, d, g and j) are comparable to those of CNTL after 60 min or 8 assimilation cycles for all five hydrometeors (first row of Fig. 10). The larger errors in the estimated parameters in Fig. 9b, e, h and k result in larger errors in q_r, q_i and q_s in certain assimilation cycles (Fig. 10g, h and i) compared to those in Fig. 9b, c and d; but the state estimation is still very good and is much better than the corresponding case without parameter estimation (the gray lines). For the experiment with relatively poor parameter estimation (black curves in Fig. 9c, f, i and l), the model state estimation (dashed curves in the third row of Fig. 10) is generally not as good as that of CNTL (solid black curves in Fig. 10) but is also much better than the case with no parameter estimation (gray curves). For this case, we can also see that in the last two assimilation cycles, the *rms* errors of the mixing ratios are actually very close to those of CNTL, except for q_s. This, we believe, is because the estimations of n_{0h} and ρ_h are poor in this experiment (Fig. 9i and l) and q_s is very sensitive to their errors, as indicated by the gray curve in Fig. 10n.

4) Simultaneous estimation of all five parameters

Using one of the two values for each parameter in Table 3 as initial guess, 32 combinations of the initial guesses were tested when estimating the five-parameter set (n_{0r}, n_{0s}, n_{0h}, ρ_s, ρ_h). In all of these experiments, 100 ensemble members were used.

The absolute ensemble mean errors of the five parameters averaged over the 32 experiments are presented in Fig. 11. The errors in n_{0h}, n_{0s} and ρ_h decrease more slowly than the corresponding ones in the four-parameter experiments (c.f. Fig. 8). At the end of the assimilation cycles, the errors of the parameters, except n_{0r}, are generally located between $2\underline{\sigma}_{P_i}$ and $3\underline{\sigma}_{P_i}$. The

estimation of n_{0r} is most successful with the absolute error of n_{0r} decreasing to $1\underline{\sigma}_{P_i}$ after six assimilation cycles and remaining close to $1\underline{\sigma}_{P_i}$ in later assimilation cycles.

Among the 32 experiments, there are 4 cases that all five parameters converge to the true values; two of them are shown in the 1st column of Fig. 12. There are a few cases in which only one of the parameters cannot converge to the truth. The black curves in the 2nd column of Fig. 12 represent one of such examples, with the error in ρ_h remaining larger than $1\underline{\sigma}_{P_i}$ in Fig. 12n. In other experiments, two or three parameters have problem converging to their true values. The poorly estimated parameters could be (n_{0h}, ρ_h) (e.g., gray curves in Fig. 12h and n); (n_{0s}, ρ_s) (e.g., black curves in Fig. 12f and l); or (n_{0h}, n_{0s}, ρ_h) (e.g., gray curves in Fig. 12f, i and o). Similar to what was found in the four-parameter experiments; n_{0r} always converges to the true value, no matter how poorly the other parameters are estimated. As in the four-parameter estimation case, the parameter estimation always improves that state estimation, even when the parameter estimation is not very accurate (not shown).

c. Data selection

In this study, we found that the data selection procedure is essential for successful parameter estimation. Its effect appears to be similar to the 'covariance localization' used for state estimation. The covariance localization is applied to avoid the influence of unreliable covariances at large distances from the observations due to sampling errors related to relatively small ensemble sizes. As a result, the model state at each grid point is only influenced by observation data found within certain range. With our data selection procedure, the estimated parameters are only influenced by the data from which the parameters are most likely to be identified, based on their correlations with the parameters. Both techniques act to alleviate filter

divergence. Aksoy et al. (2006a) offered a 'spatial updating' technique for their estimation of an eddy mixing coefficient used in a PBL scheme. With their method, the global mixing coefficient was treated and updated locally; the average of the local estimations was taken as the finial estimate of this parameter. Such a technique also helps alleviate filter divergence, but it may be more useful for parameters whose impacts are more spatially homogeneous.

Fig. 13 shows the spatial distributions of the reflectivity data that were selected in the single-parameter estimation experiments that used 40 ensemble members. When only 30 data were used, the selected data (circles in Fig. 13) are mainly concentrated in the anvil or anvil precipitation region for most of the parameters. A number of data within the convective region are selected for the estimation of n_{0r} and ρ_h. When the number of data increases to 60, most of the additional data (triangles in Fig. 13) are still located in the similar regions. These regions occupied by high-correlation data basically coincide with the high sensitivity regions found in Part I for these individual parameters (c.f. Fig. 6 of Part I). At earlier assimilation times, e.g., at 40 minutes, the selected data are found in the anvil precipitation regions for n_{0h}, n_{0s}, ρ_h and ρ_s (not shown).

The correlations at the selected data points generally increase with time. For single parameter estimation experiment, the maximum and minimum correlations of the selected data for all five parameters are around 0.6 and 0.3, respectively when 30 data are selected. At the time shown in Fig. 13, the correlations are all above 0.8 for n_{0h} and above 0.7 for n_{0s} and ρ_h, no matter whether 30 or 60 data are selected. The correlations are lower for n_{0r} and ρ_s. We also checked the correlations for the five-parameter estimation experiments. The correlations averaged over the 32 experiments are significantly smaller than those found in the single-parameter experiments, with larger decreases found for n_{0h} and ρ_h. The maximum correlations for all five parameters are no

larger than 0.6 most of the time. The differences between the maximum and minimum correlations vary between 0.1 and 0.15 for most parameters in the 30 data case. For n_{0r}, the difference varies from 0.15 to 0.2. The difference between the minimum correlations of the 30 and 60 data cases is less than 0.05 most of the time in all single-parameter and five-parameter estimation experiments. These results again indicate the increased difficulties when multiple parameters are estimated simultaneously. It also says that the correlation information is very useful for determining the value of observations for parameter estimation.

For covariance localization applied for state estimation, the optimal localization length scale normally increases as ensemble size increases (e.g., Hamill et al. 2001), because a larger ensemble reduces sampling errors. It is likely that the optimal data selection, a form of covariance localization, depends on the ensemble size. When using 100 ensemble members for multiple parameter estimation, we also tested up to 100 data. We did not find significant difference in the estimation as the number of selected data is increased from 30 to 70. The estimation became worse when more than 70 were used. For this reason, the same number (30) of data is used in used in all experiments shown.

4. Further discussion on parameter identifiability

In this section, we return to the issue of parameter identifiability and discuss some factors that might affect the parameter estimation using the EnKF method.

First, whether the uncertain parameters are identifiable is ultimately determined by whether the inverse problem has a unique solution. A parameter is said to be least square identifiable if the least square performance or cost function for identifying the parameter has a unique minimum in a given region and if the minimization is continuously dependent on the measurement errors (Sun et al. 2001). The EnKF algorithm does not explicitly minimize the

performance function, which usually measures the difference between the model solution and the observations, but the adjustment made to the prior estimate in the EnKF is proportional to that difference. If different values of a single parameter or different combinations of multiple parameters result in the same model solution or system response in terms of observed quantities, then a correct parameter estimation cannot be guaranteed because multiple possible solutions exist.

Since it has been shown that single parameters can always be estimated with good enough accuracies because of the unique global minima of the response functions, we further discuss the identifiability of multiple-parameter sets only. The results of four- and five-parameter sets suggest that multiple local minima do exist, which is not surprising because of the high nonlinearity of the microphysical processes and their interactions with the model dynamics. The multiple minima could significantly impact the estimation of multiple parameters. What is interesting to us is that in the experiments with relatively poor estimations in the four-parameter case, n_{0h} and ρ_h always converge to values that are smaller than their true values in tandem (e.g. Fig. 9i and Fig. 9l). In 11 of the 32 estimation experiments in the five-parameter case, the estimated n_{0h} and ρ_h are significantly smaller (absolute error $> 3\underline{\sigma}_{P_i}$) than their true values, and within 10 of the 11, the estimated n_{0s} is also smaller than its true value. Further, the evolutions of the estimated n_{0h}, ρ_h and n_{0s} are similar in those experiments, as can be seen in Fig. 12f, i and o.

Fig. 14 shows the correlations between radar reflectivity and the five individual parameters, which are calculated from the prior (5-minute forecast) ensemble at 70 min. The results shown are from single-parameter estimation experiments. Here, we try to understand the possible model responses in terms of reflectivity to the combined errors in the five parameters, from the correlation information. Comparing Fig. 14a, f with Fig. 14d, i, we can see that the

correlations are similar in pattern, but the signs are reversed. This means if a smaller n_{0h} results in a smaller reflectivity value in the southern anvil region (positive correlations in Fig. 14f), a smaller ρ_h can compensate for the reduction in reflectivity in that region (negative correlations in Fig. 14i). The correlation with n_{0s} also shows a reversed pattern with that with n_{0h} in the anvil region. Therefore, the change in Z in the anvil due to the change in n_{0h} can be somewhat compensated by the change in n_{0s} of the same sign. Similarly, the increase in Z at the low-level convective region due to a smaller ρ_h (Fig. 14d) can be compensated for by a smaller n_{0h} (Fig. 14a). The increase in Z at the southern part of the anvil region due to a smaller ρ_h can be compensated for by a smaller n_{0s} (negative correlations in Fig. 14b). Therefore, the errors of n_{0h}, ρ_h and n_{0s} can be combined in such a way (e.g., with all of them being smaller than their true values) that the difference between the model solution and the observations is small in terms of Z. In another word, such a combination could result in values of the response function that are close to the minimum for the multi-parameter case. Even though the correlations are still meaningful and the filter can adjust the parameters in the right directions, the end values of parameter estimation may not be correct because the response function is already reduced to be close to the minimum. As far as the estimation system, the response function has been minimized.

In the five-parameter experiments, if neither n_{0h} nor ρ_h converges to the true values, they usually have the same bias. If neither n_{0s} nor ρ_s converges to the true values, their biases are usually reversed in sign. This is also true for the estimation of (n_{0s}, ρ_s) as shown in Fig. 6. Based on the correlation information, similar explanations can be applied to these situations and to the estimation of other multiple-parameter experiments. In all multiple parameter estimation experiments that involve n_{0r}, n_{0r} always converges to the true value. This is probably because the model responds more independently to the changes in n_{0r}, as can be seen from Fig. 13. The

locations of the selected data indicate the regions that correspond to the most important model responses to the parameter errors. The data selected for the estimation of n_{0r} are indeed located more differently from those for other parameters (Fig. 13). From Fig. 13 we can also see that the data selected for n_{0h} and ρ_h are more different from each other than the data selected for n_{0s} and ρ_s, which indicate that the model responses to the errors in n_{0s} and ρ_s are more likely to cancel each other. This probably explains why the estimation of (n_{0s}, ρ_s) together is less satisfactory than the estimation of (n_{0h}, ρ_h) together.

The identifiability of the parameters depends not only on the uniqueness of the inverse solution but also on the quality of observational data. This dependence can be clearly seen in Fig. 7 and Fig. 8. The dashed curves represent the average absolute errors of the parameters estimated using 'error-free' data. Although errors were not added into the simulated data in these experiments, the same observation errors, i.e., 1 m s^{-1} for V_r and 3 dBZ for Z, were assumed during the assimilation. The estimated parameters are closer to their true values when the observations are error free. For the three-parameter estimation experiments, the errors of all three intercept parameters are reduced to 1 $\underline{\sigma}_{P_i}$ within 50 minutes and kept below 1 $\underline{\sigma}_{P_i}$ in the later assimilation cycles (Fig. 7b, d, f). For the four-parameter estimation experiments, the errors of all four parameters are decreased below 1 $\underline{\sigma}_{P_i}$ at the end of the assimilation cycles. We repeated the five-parameter experiments with error-free data for 6 out of the 32 cases that had poor parameter estimations. Using error-free data, the parameters converge to the true values perfectly in 5 of the 6 cases (not shown). This suggests a significant sensitivity to the observation errors.

Parameter estimation using the EnKF method is also found in this study to be very sensitive to the random realization of the initial ensemble. For single-parameter estimations, different realizations lead to different convergence rates (Fig. 2). For multiple parameter

estimations, it even affects the success of the estimation. Fig. 15 shows the results of four 5-parameter estimation experiments that differ only in the realization of the initial parameter ensemble, for the four parameters that often have problem. In two of the experiments, all five parameters (n_{0r} is not shown) converge to their true values (solid black and black dashed curves in Fig. 15) but the convergence rates of n_{0h} and ρ_h are very different. In the other two experiments, two or three of the parameters cannot converge to the true values. The random numbers sampled for the parameters apparently directly affect the model response and the error covariances estimated from the ensemble. Better and more physical sampling strategies may need to be developed for future applications.

5. Summary and conclusions

The possibility of correcting model errors associated with uncertain microphysical parameters found in a popular single-moment ice microphysics scheme through parameter estimation is investigated. The EnKF method and radar data are used for the parameter as well as state estimations. The parameters estimated include the intercept parameters of the assumed exponential drop size distributions (DSDs) for rain, snow and hail, and the densities of hail and snow. Sensitivity analyses were performed for individual parameters in Part I, together with discussions on the parameter identifiability, to provide guidance for the parameter estimation experiments. In this second part, we use the EnKF method to estimate those microphysical parameters individually or in different combinations. The identifiability of multiple parameters is further investigated based on the estimation results.

The experiments showed that when the microphysical parameters are estimated individually (with other parameters being perfect), they all can closely converge to their true values. This is not surprising because the sensitivity analyses in Part I indicate that the inverse

problems for single-parameter estimation have unique solutions. For this case of well posed problem, the EnKF can be used effectively for simultaneous state and parameter estimations.

The results of multiple-parameter estimations are not as good as those of single-parameter estimations, but the results estimating parameter sets (n_{0h}, ρ_h), (n_{0r}, n_{0s}, n_{0h}) and (n_{0r}, n_{0s}, n_{0h}, ρ_h) are very encouraging. The difficulty in estimating some parameters appears to be due to the fact that the model responses to the errors in different parameters can cancel each other so that combinations of parameters with different errors can still result in a good fit of the model solution to the observations, rendering the solution to the parameter estimation problem non-unique. Further, estimation can be sensitive to the quality of the observational data. It is found that the realization of the initial parameter ensemble can also affect the parameter estimation significantly, especially in the multi-parameter estimation cases. In such cases, increasing the ensemble size (e.g., from 40 to 100) help improve the accuracy and robustness of the estimation.

In this study, we applied the parameter estimation to a simulated supercell storm only. Some parameters or combinations of the parameters may be more or less identifiable in other types of convective systems. For example, mature squall lines usually contain more stratiform precipitation regions that develop and evolve over a longer period of time, which may be helpful for the parameter estimation. Additional observation types, such as those from dual-polarization radars, may be very helpful for microphysical parameter estimation because of their information content on DSDs and hydrometeor types. At least, the dual-polarization data can provide additional constraints on the inverse problem, which hopefully can improve the solution uniqueness. Work in assimilating polarimetric Doppler radar data and in including the data in microphysical parameter estimation using the EnKF is in progress (Jung et al. 2007b; Jung et al. 2007a), and initial results are encouraging.

In real applications, parameter estimation will be performed simultaneously with state estimation in continuous assimilation cycles. The latest estimation of the uncertain parameters as well as the model state should be used for subsequent forecasting. We note in the end that for real data applications, the model error in precipitation microphysics is likely to be larger than what is considered here. The estimation of other microphysical parameters, such as the fall speed coefficients and collection efficiencies, and other uncertain parameters involved in microphysical conversion processes, are worthy of investigations too. Additional difficulties are expected when more uncertainties in microphysics scheme are considered. Furthermore, other sources of model error can make parameter estimation more difficult. Parameter estimation in the presence of other sources of error is an interesting topic for future studies. What is encouraging is that even in the most difficult cases considered in this study, the errors of the estimated parameters are usually significantly smaller than their first guess errors, and the results of state estimation are almost always improved when simultaneous parameter estimation is performed. It is clear that the radar reflectivity data are effective in constraining errors in the microphysical parameters.

Acknowledgement: This work was primarily supported by NSF grants ATM-0129892 and ATM-0530814. M. Xue was further supported by NSF grants EEC-0313747, ATM-0331594 and, ATM-0608168 and by grants from Chinese Academy of Sciences (No. 2004-2-7) and Chinese Natural Science Foundation (No. 40620120437). Comments and suggestions by anonymous reviewers significantly improved our paper.

References

Aksoy, A., F. Zhang, and J. W. Nielsen-Gammon, 2006a: Ensemble-based simultaneous state and parameter estimation with MM5. *Geophys. Res. Letters*, **33,** L12801, doi:10.1029/2006GL026186.

Aksoy, A., F. Zhang, and J. W. Nielsen-Gammon, 2006b: Ensemble-based simutaneous state and parameter estimation in a two-dimensional sea breeze model. *Mon. Wea. Rev.*, **134,** 2951-2970.

Anderson, J. L., 2001: An ensemble adjustment Kalman filter for data assimilation. *Mon. Wea. Rev.*, **129,** 2884-2903.

Annan, J. D. and J. C. Hargreaves, 2004: Efficient parameter estimation for a highly chaotic system. *Tellus*, **56A,** 520-526.

Annan, J. D., D. J. Lunt, J. C. Hargreaves, and P. J. Valdes, 2005a: Parameter estimation in an atmospheric GCM using the ensemble Kalman filter. *Nonlinear Processes in Geophysics*, **12,** 363-371.

Annan, J. D., J. C. Hargreaves, N. R. Edwards, and R. Marsh, 2005b: Parameter estimation in an intermediate complexity earth system model using an ensemble Kalman filter. *Ocean Modelling*, **8,** 135-154.

Bishop, C. H., B. J. Etherton, and S. J. Majumdar, 2001: Adaptive sampling with the ensemble transform Kalman filter. Part I: Theoretical aspects. *Mon. Wea. Rev.*, **129,** 420.

Burgers, G., P. J. v. Leeuwen, and G. Evensen, 1998: Analysis scheme in the ensemble Kalman filter. *Mon. Wea. Rev.*, **126,** 1719-1724.

Crook, N. A., D. Dowell, J. Sun, and Y. Zhang, 2004: Assimilation of radar observations of a supercell storm using 4DVar: Parameter retrieval experiments. 22nd Conference on

Severe Local Storms, Hyannis, Massachusetts, Amer. Meteor. Soc., CDROM 8A.2.

Dee, D. P., 1995: On-line estimation of error covariance parameters for atmospheric data assimilation. *Mon. Wea. Rev.*, **123,** 112-81145.

Dowell, D., F. Zhang, L. J. Wicker, C. Snyder, and N. A. Crook, 2004: Wind and temperature retrievals in the 17 May 1981 Arcadia, Oklahoma supercell: Ensemble Kalman filter experiments. *Mon. Wea. Rev.*, **132,** 1982-2005.

Evensen, G., 1994: Sequential data assimilation with a nonlinear quasi-geostrophic model using Monte Carlo methods to forecast error statistics. *J. Geophys. Res.*, **99(C5),** 10 143-10 162.

Evensen, G., 2003: The ensemble Kalman filter: Theoretical formulation and practical implementation. *Ocean Dynamics*, **53,** 343-367.

Gilmore, M. S., J. M. Straka, and E. N. Rasmussen, 2004: Precipitation uncertainty due to variations in precipitation particle parameters within a simple microphysics scheme. *Mon. Wea. Rev.*, **132,** 2610-2627.

Hacker, J. P. and C. Snyder, 2005: Ensemble Kalman filter assimilation of fixed screen-height observations in a parameterized PBL. *Mon. Wea. Rev.*, **133,** 3260-3275.

Hamill, T. M., J. S. Whitaker, and C. Snyder, 2001: Distance-dependent filtering of background error covariance estimates in an ensemble Kalman filter. *Mon. Wea. Rev.*, **129,** 2776-2790.

Hansen, J. A., 2002: Accounting for Model Error in Ensemble-Based State Estimation and Forecasting. *Mon. Wea. Rev.*, **130,** 2373-2391.

Hao, Z. and M. Ghil, 1995: Sequential parameter estimation for a coupled ocean-atmosphere model. Proceeding, WMO 2nd International Symposium on Assimilatoin of Observations

in Meteorology and Oceanography, Tokyo, Japan, 181-186.

Houtekamer, P. L. and H. L. Mitchell, 1998: Data assimilation using an ensemble Kalman filter technique. *Mon. Wea. Rev.*, **126,** 796-811.

Houtekamer, P. L. and H. L. Mitchell, 2001: A sequential ensemble Kalman filter for atmospheric data assimilation. *Mon. Wea. Rev.*, **129,** 123-137.

Houtekamer, P. L., H. L. Mitchell, G. Pellerin, M. Buehner, M. Charron, L. Spacek, and B. Hansen, 2005: Atmospheric data assimilation with an ensemble Kalman filter: Results with real observations. *Mon. Wea. Rev.*, **133,** 604-620.

Jung, Y., G. Zhang, and M. Xue, 2007a: Assimilation of simulated polarimetric radar data for a convective storm using ensemble Kalman filter. Part I: Observation operators for reflectivity and polarimetric variables. *Mon. Wea. Rev.***,** Under reivew.

Jung, Y., M. Xue, G. Zhang, and J. Straka, 2007b: Assimilation of simulated polarimetric radar data for a convective storm using ensemble Kalman filter. Part II: Impact of polarimetric data on storm analysis. *Mon. Wea. Rev.***,** Under review.

Kivman, G. A., 2003: Sequential parameter estimation for stochastic systems. *Nonlinear Processes in Geophysics*, **10,** 253-259.

Lin, Y.-L., R. D. Farley, and H. D. Orville, 1983: Bulk parameterization of the snow field in a cloud model. *J. Climate Appl. Meteor.*, **22,** 1065-1092.

Ray, P. S., B. Johnson, K. W. Johnson, J. S. Bradberry, J. J. Stephens, K. K. Wagner, R. B. Wilhelmson, and J. B. Klemp, 1981: The morphology of severe tornadic storms on 20 May 1977. *J. Atmos. Sci.*, **38,** 1643-1663.

Snyder, C. and F. Zhang, 2003: Assimilation of simulated Doppler radar observations with an ensemble Kalman filter. *Mon. Wea. Rev.*, **131,** 1663-1677.

Sun, N., N.-Z. Sun, M. Elimelech, and J. N. Ryan, 2001: Sensitivity analysis and parameter identifiability for colloid transport in geochemically heterogeneous porous media. *Water Resour. Res.*, **37,** 209-222.

Tong, M., 2006: Ensemble Kalman filer assimilation of Doppler radar data for the initialization and prediction of convective storms, Ph.D. Dissertation, School of Meteorology, University of Oklahoma, 243 pp.

Tong, M. and M. Xue, 2005a: Ensemble Kalman filter assimilation of Doppler radar data with a compressible nonhydrostatic model: OSS Experiments. *Mon. Wea. Rev.*, **133,** 1789-1807.

Tong, M. and M. Xue, 2005b: Simultaneous retrieval of microphysical parameters and atmospheric state variables with radar data and ensemble Kalman filter method. Preprint, 17th Conf. Num. Wea. Pred., Washington DC, Amer. Meteor. Soc., CDROM P1.30.

Tong, M. and M. Xue, 2007: Simultaneous estimation of microphysical parameters and atmospheric state with radar data and ensemble square-root Kalman filter. Part I: Sensitivity analysis and parameter identifiability *Mon. Wea. Rev.***,** Accepted.

Whitaker, J. S. and T. M. Hamill, 2002: Ensemble data assimilation without perturbed observations. *Mon. Wea. Rev.*, **130,** 1913-1924.

Xue, M., K. K. Droegemeier, and V. Wong, 2000: The Advanced Regional Prediction System (ARPS) - A multiscale nonhydrostatic atmospheric simulation and prediction tool. Part I: Model dynamics and verification. *Meteor. Atmos. Physics*, **75,** 161-193.

Xue, M., M. Tong, and K. K. Droegemeier, 2006: An OSSE framework based on the ensemble square-root Kalman filter for evaluating impact of data from radar networks on thunderstorm analysis and forecast. *J. Atmos. Ocean Tech.*, **23,** 46–66.

Xue, M., D.-H. Wang, J.-D. Gao, K. Brewster, and K. K. Droegemeier, 2003: The Advanced

Regional Prediction System (ARPS), storm-scale numerical weather prediction and data assimilation. *Meteor. Atmos. Physics*, **82,** 139-170.

Xue, M., K. K. Droegemeier, V. Wong, A. Shapiro, K. Brewster, F. Carr, D. Weber, Y. Liu, and D.-H. Wang, 2001: The Advanced Regional Prediction System (ARPS) - A multiscale nonhydrostatic atmospheric simulation and prediction tool. Part II: Model physics and applications. *Meteor. Atmos. Phy.*, **76,** 143-165.

Yu, L. and J. J. O'Brien, 1991: Variational estimation of the wind stress drag coefficient and the oceanic eddy viscosity profile. *J. Phys. Oceanogr.*, **21,** 709-719.

Zhang, F., C. Snyder, and J. Sun, 2004: Impacts of initial estimate and observations on the convective-scale data assimilation with an ensemble Kalman filter. *Mon. Wea. Rev.*, **132,** 1238-1253.

Zou, X., I. M. Navon, and F. X. Le Dimet, 1992: An optimal nudging data assimilation scheme using parameter estimation. *Quart. J. Roy. Meteor. Soc.*, **118,** 1163-1186.

List of Figures

Fig. 1. The evolution of the parameter distribution from single-parameter estimation experiments through the assimilation cycles for n_{0h} (a)-(c), n_{0s} (d)-(f), n_{0r} (g)-(i), ρ_s (j)-(l), and ρ_h (m)-(o). The three columns are for different initial guesses of the parameters which are given in Table 2. The straight horizontal lines indicate the true values of the parameters. The stair-like curves indicate the ensemble mean (solid) and the 1 σ_{P_i} ensemble width (dashed) of the estimated parameter before and after analysis.

Fig. 2. The evolution of the ensemble means of estimated parameter for five single-parameter estimation experiments (shown in different line patterns) starting from the same initial guess but different realizations of the initial parameter ensemble, the intercept parameter of hail/graupel n_{0h} (a), and the density of snow ρ_s (b).

Fig. 3. The rms errors of the ensemble-mean forecast and analysis, averaged over points at which the reflectivity is greater than 10 dBZ for q_c (the 1st column), q_r (the 2nd column), q_i (the 3rd column), q_s (the 4th column), q_h (the 5th column), for the CNTL data assimilation experiment (black), parameter estimation experiments (dashed) and data assimilation experiments with imperfect parameter kept throughout the assimilation cycles (gray). The experiments shown have (wrong) initial guesses of ρ_h = 400 kg m^{-3} (a-e), $n_{0r} = 8\times10^7$ m^{-4} (f-j), and ρ_s = 400 kg m^{-3} (k-o), which correspond to the experiments in Fig. 1m, Fig. 1i and Fig. 1l.

Fig. 4. The evolution of the parameter distributions (solid curves: ensemble mean, dashed curves: 1 σ_{P_i} ensemble width) vs. true parameter values (straight lines) for experiments simultaneously estimating n_{0h} (the upper row) and ρ_h (the lower row). The four columns

are for different initial guesses of the parameters, which are (n_{0h} = 4×10^6 m^{-4}, ρ_h = 400 kg m^{-3}) (a, e); (n_{0h} = 4×10^6 m^{-4}, ρ_h = 700 kg m^{-3}) (b, f); (n_{0h} = 4×10^5 m^{-4}, ρ_h = 400 kg m^{-3}) (c, g); and (n_{0h} = 4×10^5 m^{-4}, ρ_h = 700 kg m^{-3}) (d, h).

Fig. 5. The same as Fig. 3, but for the two-parameter set (n_{0h}, ρ_h). The experiments shown have initial guesses of (n_{0h}, ρ_h) = (4×10^6 m^{-4}, 400 kg m^{-3}) (first row), and (n_{0h}, ρ_h) = (4×10^5 m^{-4}, 700 kg m^{-3}) (second row), which correspond to the experiments in the 1st and the 4th column of Fig. 4, respectively.

Fig. 6. As Fig. 4 but for experiments simultaneously estimating (n_{0s}, ρ_s) starting from four different initial guesses, which are (n_{0s} = 3×10^7 m^{-4}, ρ_s = 300 kg m^{-3}) (a, e); (n_{0s} = 3×10^7 m^{-4}, ρ_s = 50 kg m^{-3}) (b, f); (n_{0s} = 7×10^5 m^{-4}, ρ_s = 300 kg m^{-3}) (c, g); and (n_{0s} = 7×10^5 m^{-4}, ρ_s = 50 kg m^{-3}) (d, h). The gray and black curves are for experiments using 40 and 100 ensemble members, respectively.

Fig. 7. The left column shows the ensemble means of 10log$_{10}$(n_{0r}) (a), 10log$_{10}$(n_{0s}) (c), 10log$_{10}$(n_{0h}) (e), of the experiments estimating three intercept parameters simultaneously using 40 ensemble members and 'error containing' data, for 8 experiments starting from different initial guesses that are different combinations of the values listed in Table 3. The right column shows the absolute ensemble mean errors for the corresponding parameters averaged over the 8 experiments using 40 ensemble members with 'error containing' data (solid gray), 100 members with 'error containing' data (solid black), and 100 members with 'error-free' data (black dashed).

Fig. 8. The evolution of the average ensemble-mean absolute error of 10log$_{10}$(n_{0r}) (a), 10log$_{10}$(n_{0s}) (b), 10log$_{10}$(n_{0h}) (c), and 10log$_{10}$(ρ_h) (d), calculated from the 16 experiments with different initial guesses that simultaneously estimate (n_{0r}, n_{0s}, n_{0h}, ρ_h), using 40 ensemble

members with error-containing data (solid gray), 100 members with error-containing data (solid black), and 100 ensemble members with error-free data (black dashed).

Fig. 9. As Fig. 4 but for experiments estimating four parameters simultaneously, using 100 ensemble members. Parameters shown are for n_{0r} (a-c), n_{0s} (d-f), n_{0h} (g-i), and ρ_h (j-l) . The results of 6 (2 in each column) of a total of 16 experiments with different initial guesses of (n_{0r}, n_{0s}, n_{0h}, ρ_h) are presented, with each experiment presented by the same gray level of curves in each column.

Fig. 10. As Fig. 3 but for three four-parameter (n_{0r}, n_{0s}, n_{0h}, ρ_h) estimation experiments, starting from initial guesses of (n_{0r}, n_{0s}, n_{0h}, ρ_h) = (0.2 m^{-4}, 0.3 m^{-4}, 0.004 m^{-4}, 700 kg m^{-3}) (first row); (n_{0r}, n_{0s}, n_{0h}, ρ_h) = (0.03 m^{-4}, 0.007 m^{-4}, 0.04 m^{-4}, 400 kg m^{-3}) (second row), and (n_{0r}, n_{0s}, n_{0h}, ρ_h) = (0.03 m^{-4}, 0.3 m^{-4}, 0.04 m^{-4}, 700 kg m^{-3}) (third row), which correspond to the black curves in the 1st, 2nd and 3rd column of Fig. 9, respectively. To be consistent, 100 ensemble members are used in the control experiment shown here.

Fig. 11. The evolution of average ensemble-mean absolute errors of (a) $10\log_{10}(n_{0r})$ (solid black), $10\log_{10}(n_{0s})$ (solid gray), $10\log_{10}(n_{0h})$ (black dashed), and (b) $10\log_{10}(\rho_h)$ (solid gray) and $10\log_{10}(\rho_s)$ (solid black), calculated from 32 experiments starting from different initial guesses that simultaneously estimate (n_{0r}, n_{0s}, n_{0h}, ρ_h, ρ_s) using 100 ensemble members.

Fig. 12. As Fig. 4 but for experiments estimating five parameters simultaneously, using 100 ensemble members. Parameters shown are for n_{0r} (a)-(c), n_{0s} (d)-(f), n_{0h} (g)-(i), ρ_s (j)-(l), and ρ_h (m)-(o). The results of 6 of a total of 32 experiments with different initial guesses of (n_{0r}, n_{0s}, n_{0h}, ρ_h, ρ_s) are presented (2 in each column), with each experiment represented by the same gray level of curves in each column.

Fig. 13. The circles and triangles indicate the locations of the reflectivity data that were used in

the single-parameter estimation experiments, which correspond to (b), (e), (i), (l) and (m) in Fig. 1. The data points are projected to the horizontal *x*-*y* (first row) and *x*-*z* vertical (second row) planes. The circles represent the data points when 30 data are used for parameter estimation. The triangles represent the additional 30 data points when 60 data are used. The shading and thin solid contours represent composite or column maximum reflectivity of the truth simulation in *z* (a-e) and *y* (f-j) directions. The maximum and minimum values of the correlation coefficient at those data points are indicated by the plots.

Fig. 14. Correlation coefficients calculated from the forecast ensemble at $t = 70$ min from single-parameter estimation experiments. The correlation coefficients [thick solid (dashed) contours represent positive (negative) values at intervals of 0.2] between Z at the 1.5° radar elevation and n_{0h} (a), n_{0s} (b), n_{0r} (c), ρ_h (d), and ρ_s (e); and the correlation coefficients between Z at 5.3° elevation and n_{0h} (f), n_{0s} (g), n_{0r} (h), ρ_h (i), and ρ_s (j). The shading with thin solid contours shows the Z fields from the truth simulation.

Fig. 15. The evolutions of the ensemble means together with the true values (straight lines) of $10\log_{10}(n_{0h})$ (a), $10\log_{10}(n_{0s})$ (b), $10\log_{10}(\rho_h)$ (c) and $10\log_{10}(\rho_s)$ (d), from experiments estimating (n_{0r}, n_{0s}, n_{0h}, ρ_s, ρ_h) starting from (4×10^5 m^{-4}, 3×10^7 m^{-4}, 3×10^7 m^{-4}, 50 kg m^{-3}, 400 kg m^{-3}). The different line types in each panel represent experiments using different realizations of the initial parameter ensemble.

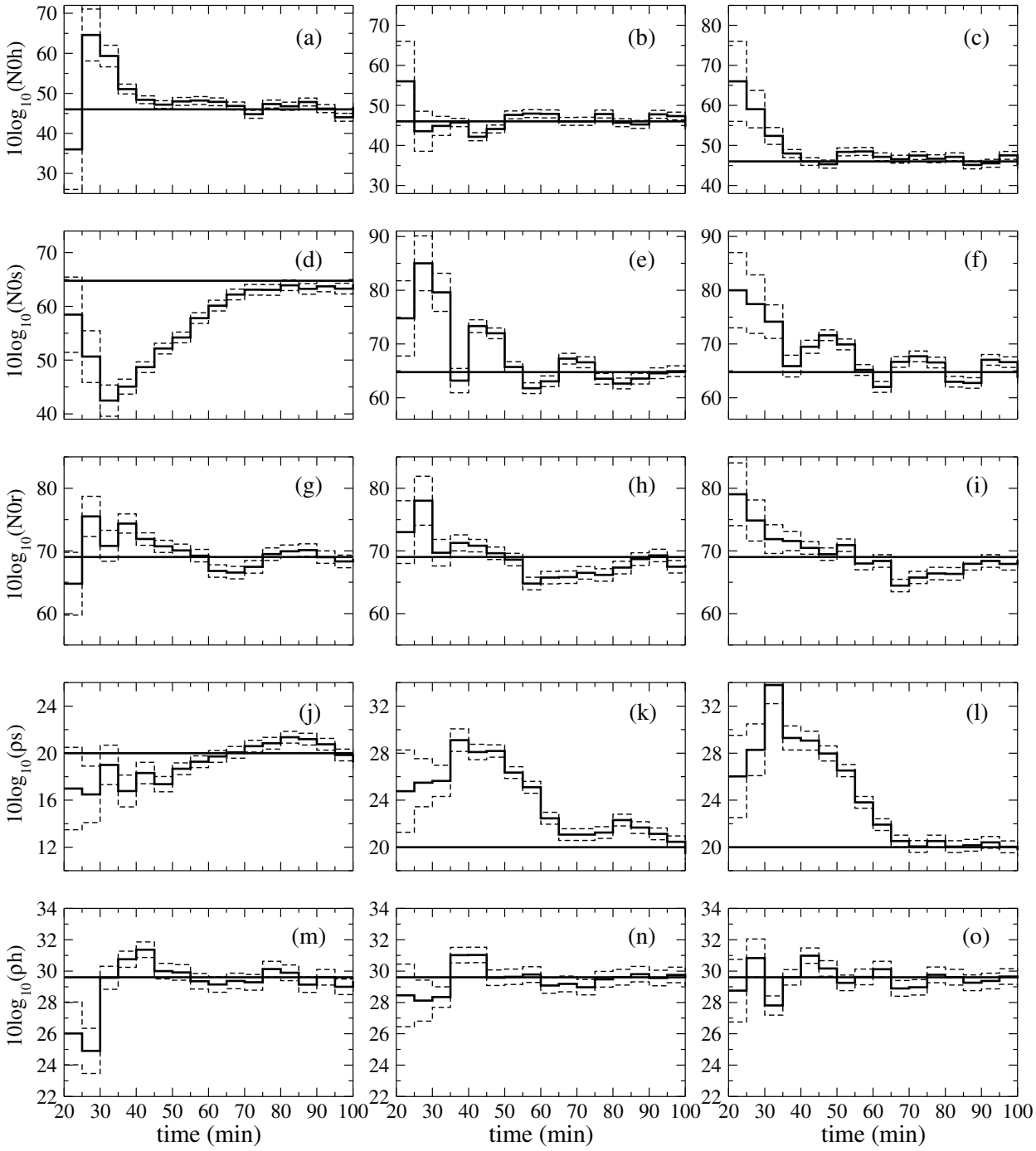

Fig. 1. The evolution of the parameter distribution from single-parameter estimation experiments through the assimilation cycles for n_{0h} (a)-(c), n_{0s} (d)-(f), n_{0r} (g)-(i), ρ_s (j)-(l), and ρ_h (m)-(o). The three columns are for different initial guesses of the parameters which are given in Table 2. The straight horizontal lines indicate the true values of the parameters. The stair-like curves indicate the ensemble mean (solid) and the 1 σ_{P_i} ensemble width (dashed) of the estimated parameter before and after analysis.

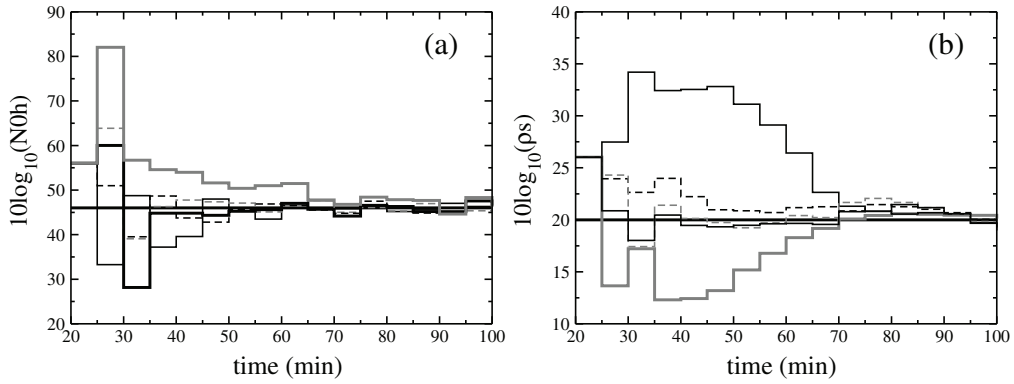

Fig. 2. The evolution of the ensemble means of estimated parameter for five single-parameter estimation experiments (shown in different line patterns) starting from the same initial guess but different realizations of the initial parameter ensemble, the intercept parameter of hail/graupel n_{0h} (a), and the density of snow ρ_s (b).

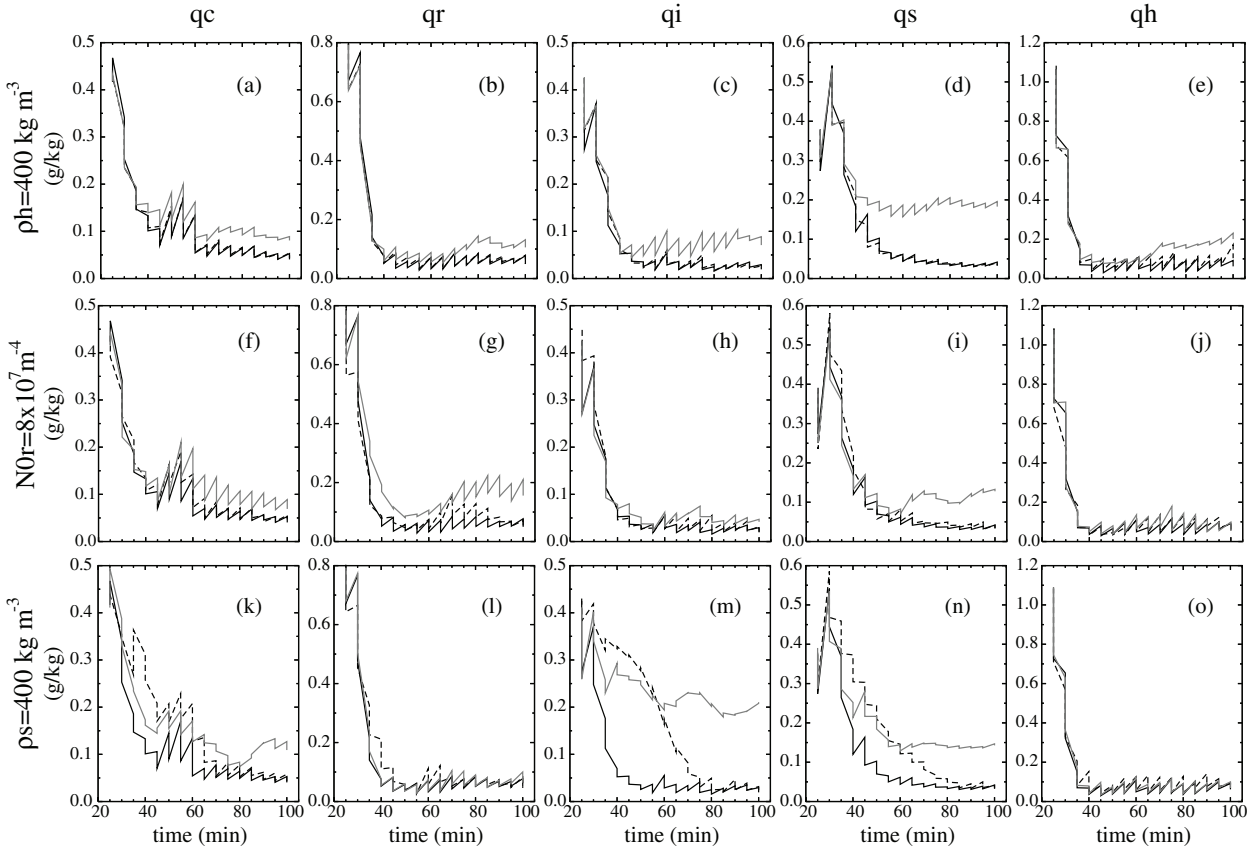

Fig. 3. The rms errors of the ensemble-mean forecast and analysis, averaged over points at which the reflectivity is greater than 10 dBZ for q_c (the 1st column), q_r (the 2nd column), q_i (the 3rd column), q_s (the 4th column), q_h (the 5th column), for the CNTL data assimilation experiment (black), parameter estimation experiments (dashed) and data assimilation experiments with imperfect parameter kept throughout the assimilation cycles (gray). The experiments shown have (wrong) initial guesses of ρ_h = 400 kg m^{-3} (a-e), n_{0r} = 8×10^7 m^{-4} (f-j), and ρ_s = 400 kg m^{-3} (k-o), which correspond to the experiments in Fig. 1m, Fig. 1i and Fig. 1l.

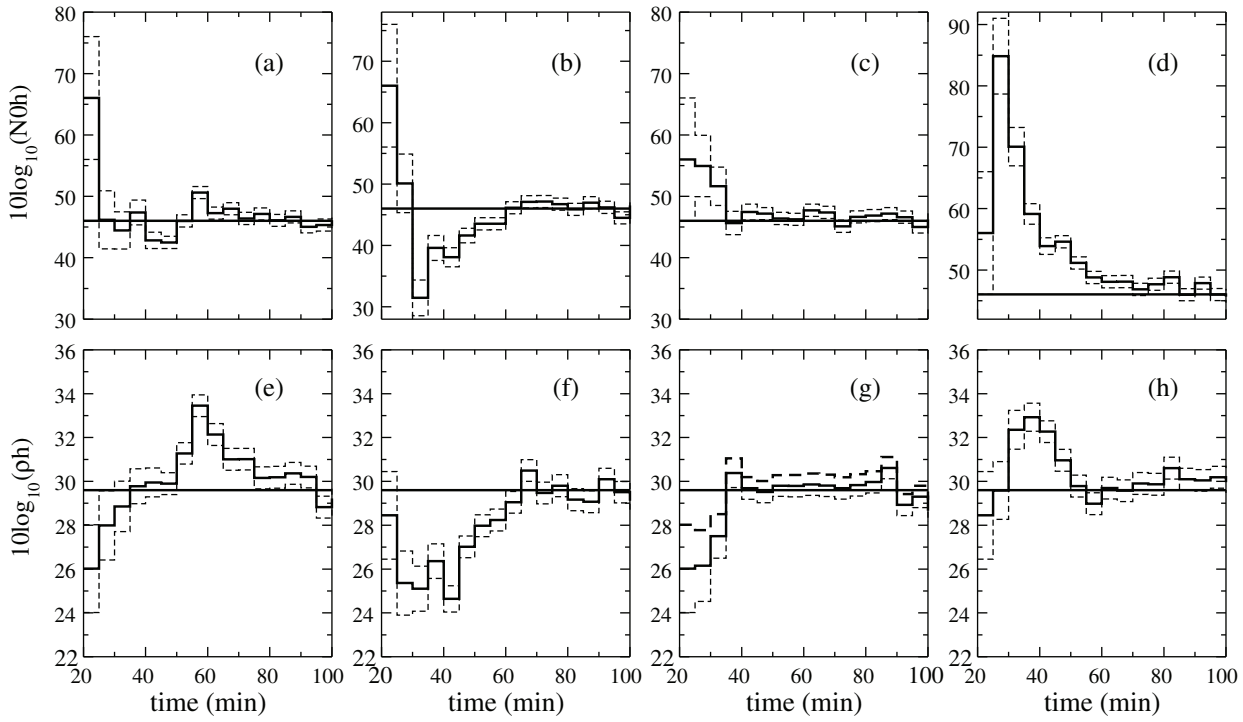

Fig. 4. The evolution of the parameter distributions (solid curves: ensemble mean, dashed curves: 1 σ_{P_i} ensemble width) vs. true parameter values (straight lines) for experiments simultaneously estimating n_{0h} (the upper row) and ρ_h (the lower row). The four columns are for different initial guesses of the parameters, which are (n_{0h} = 4×10^6 m^{-4}, ρ_h = 400 kg m^{-3}) (a, e); (n_{0h} = 4×10^6 m^{-4}, ρ_h = 700 kg m^{-3}) (b, f); (n_{0h} = 4×10^5 m^{-4}, ρ_h = 400 kg m^{-3}) (c, g); and (n_{0h} = 4×10^5 m^{-4}, ρ_h = 700 kg m^{-3}) (d, h).

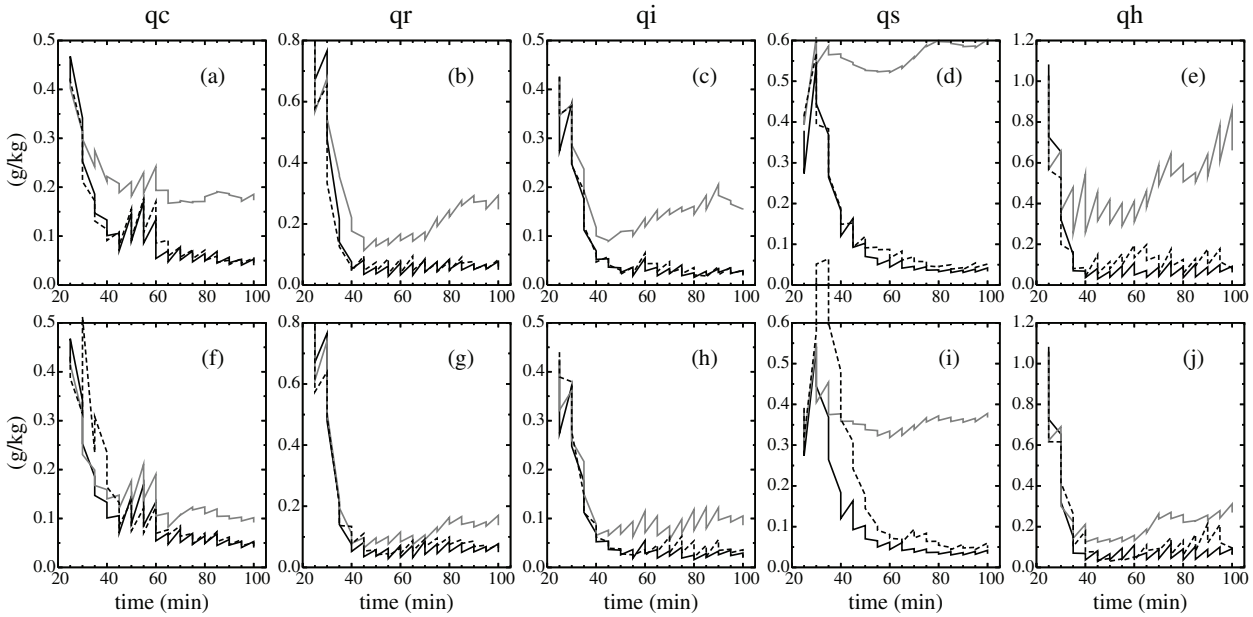

Fig. 5. The same as Fig. 3, but for the two-parameter set (n_{0h}, ρ_h). The experiments shown have initial guesses of (n_{0h}, ρ_h) = (4×10^6 m^{-4}, 400 kg m^{-3}) (first row), and (n_{0h}, ρ_h) = (4×10^5 m^{-4}, 700 kg m^{-3}) (second row), which correspond to the experiments in the 1st and the 4th column of Fig. 4, respectively.

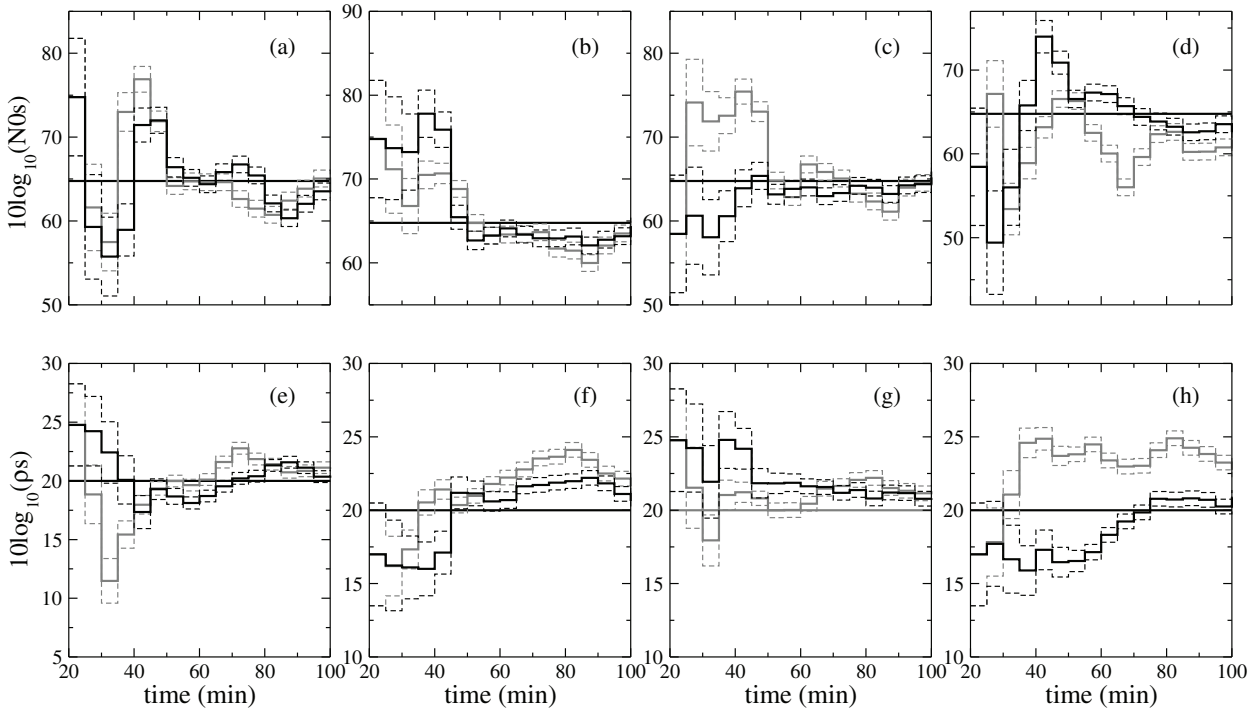

Fig. 6. As Fig. 4 but for experiments simultaneously estimating (n_{0s}, ρ_s) starting from four different initial guesses, which are ($n_{0s} = 3\times10^7$ m^{-4}, $\rho_s = 300$ kg m^{-3}) (a, e); ($n_{0s} = 3\times10^7$ m^{-4}, $\rho_s = 50$ kg m^{-3}) (b, f); ($n_{0s} = 7\times10^5$ m^{-4}, $\rho_s = 300$ kg m^{-3}) (c, g); and ($n_{0s} = 7\times10^5$ m^{-4}, $\rho_s = 50$ kg m^{-3}) (d, h). The gray and black curves are for experiments using 40 and 100 ensemble members, respectively.

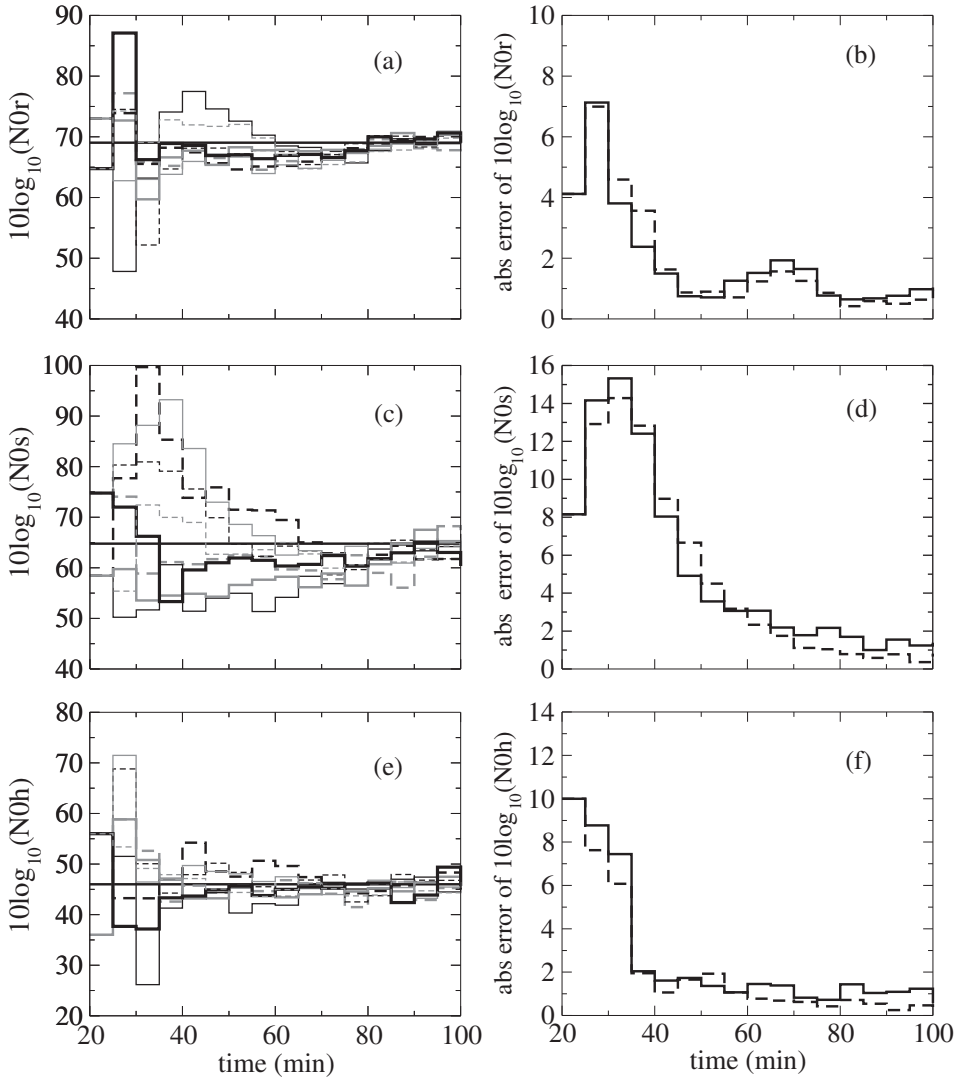

Fig. 7. The left column shows the ensemble means of $10\log_{10}(n_{0r})$ (a), $10\log_{10}(n_{0s})$ (c), $10\log_{10}(n_{0h})$ (e), of the experiments estimating three intercept parameters simultaneously using 40 ensemble members and 'error containing' data, for 8 experiments starting from different initial guesses that are different combinations of the values listed in Table 3. The right column shows the absolute ensemble mean errors for the corresponding parameters averaged over the 8 experiments using 40 ensemble members with 'error containing' data (solid gray), 100 members with 'error containing' data (solid black), and 100 members with 'error-free' data (black dashed).

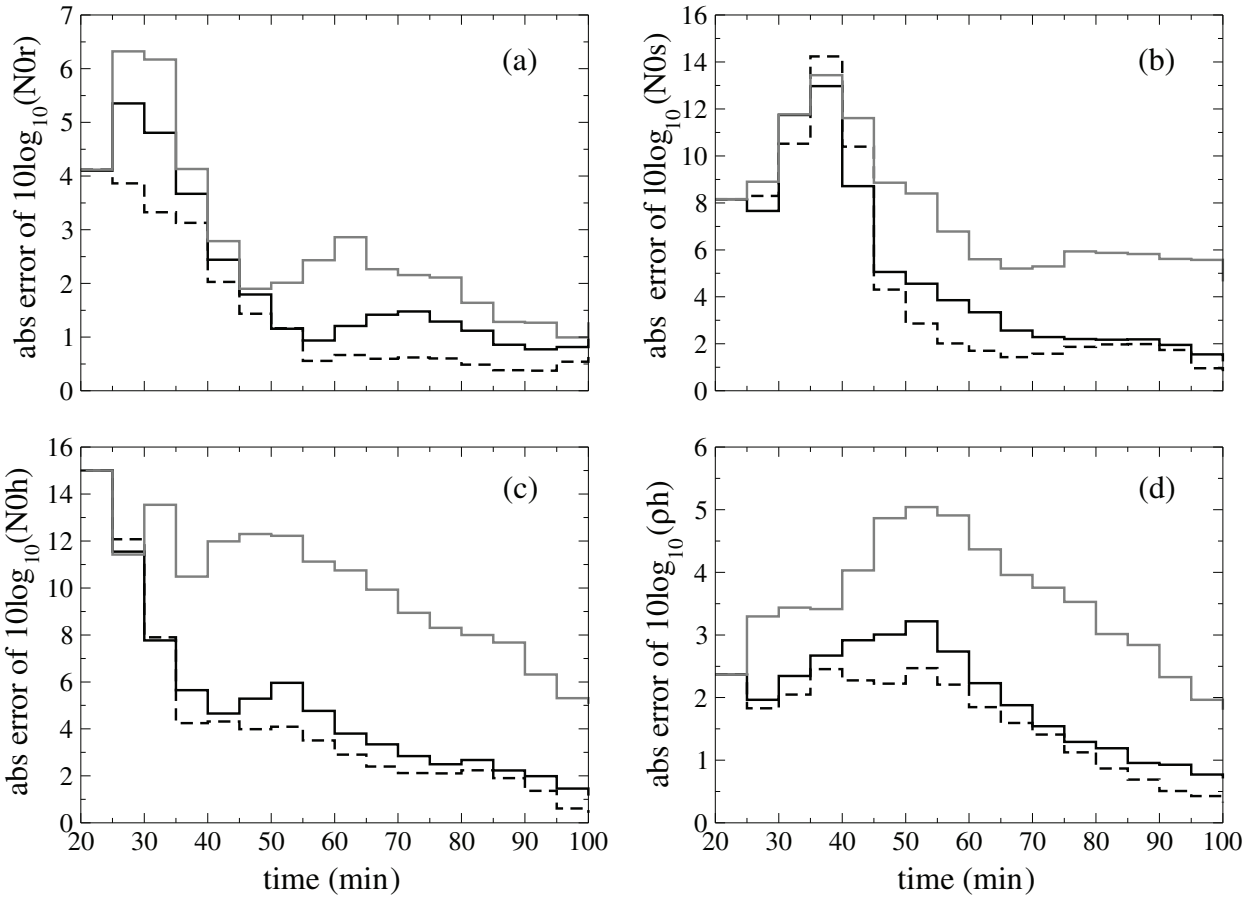

Fig. 8. The evolution of the average ensemble-mean absolute error of $10\log_{10}(n_{0r})$ (a), $10\log_{10}(n_{0s})$ (b), $10\log_{10}(n_{0h})$ (c), and $10\log_{10}(\rho_h)$ (d), calculated from the 16 experiments with different initial guesses that simultaneously estimate (n_{0r}, n_{0s}, n_{0h}, ρ_h), using 40 ensemble members with error-containing data (solid gray), 100 members with error-containing data (solid black), and 100 ensemble members with error-free data (black dashed).

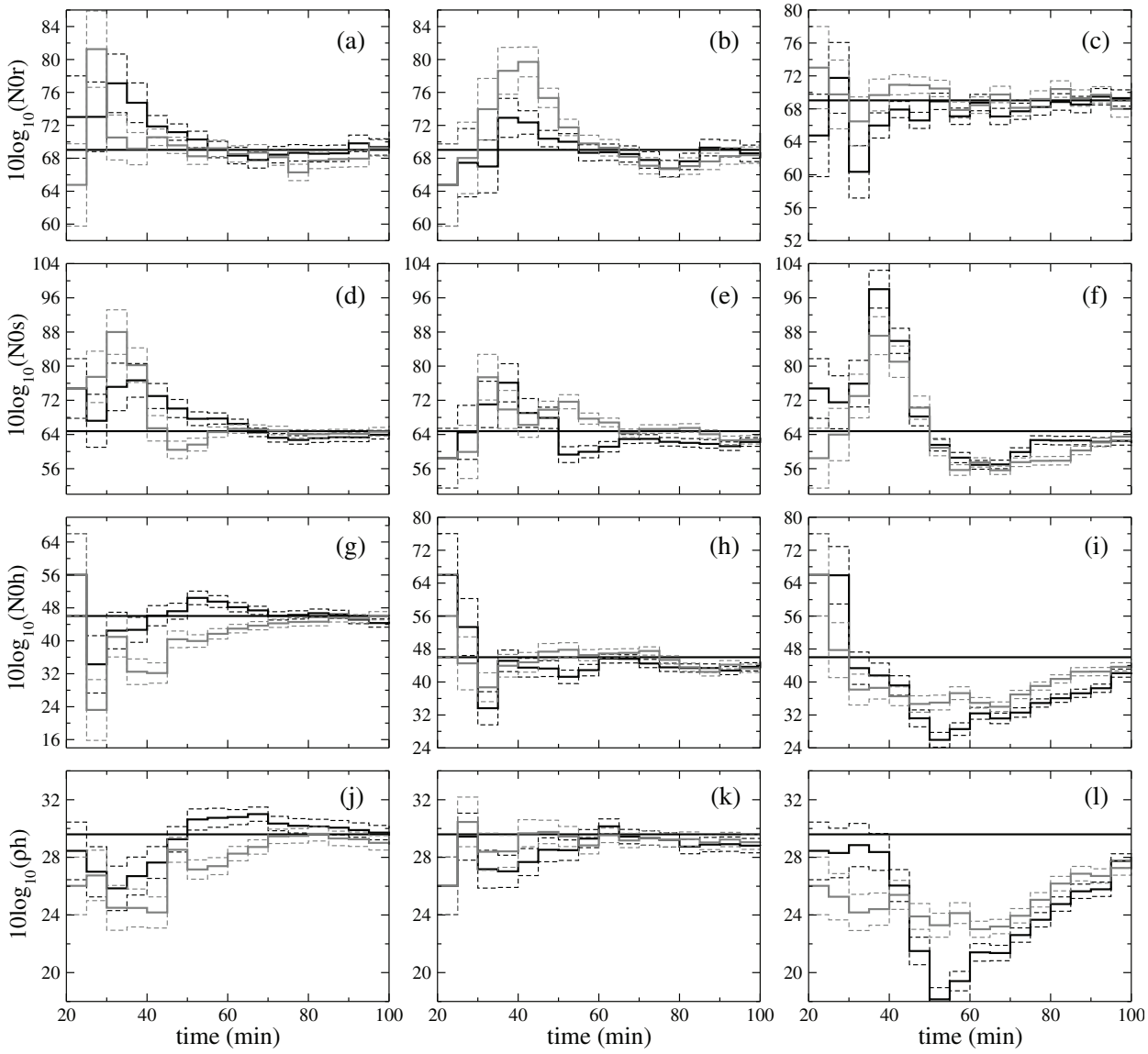

Fig. 9. As Fig. 4 but for experiments estimating four parameters simultaneously, using 100 ensemble members. Parameters shown are for n_{0r} (a-c), n_{0s} (d-f), n_{0h} (g-i), and ρ_h (j-l) . The results of 6 (2 in each column) of a total of 16 experiments with different initial guesses of (n_{0r}, n_{0s}, n_{0h}, ρ_h) are presented, with each experiment presented by the same gray level of curves in each column.

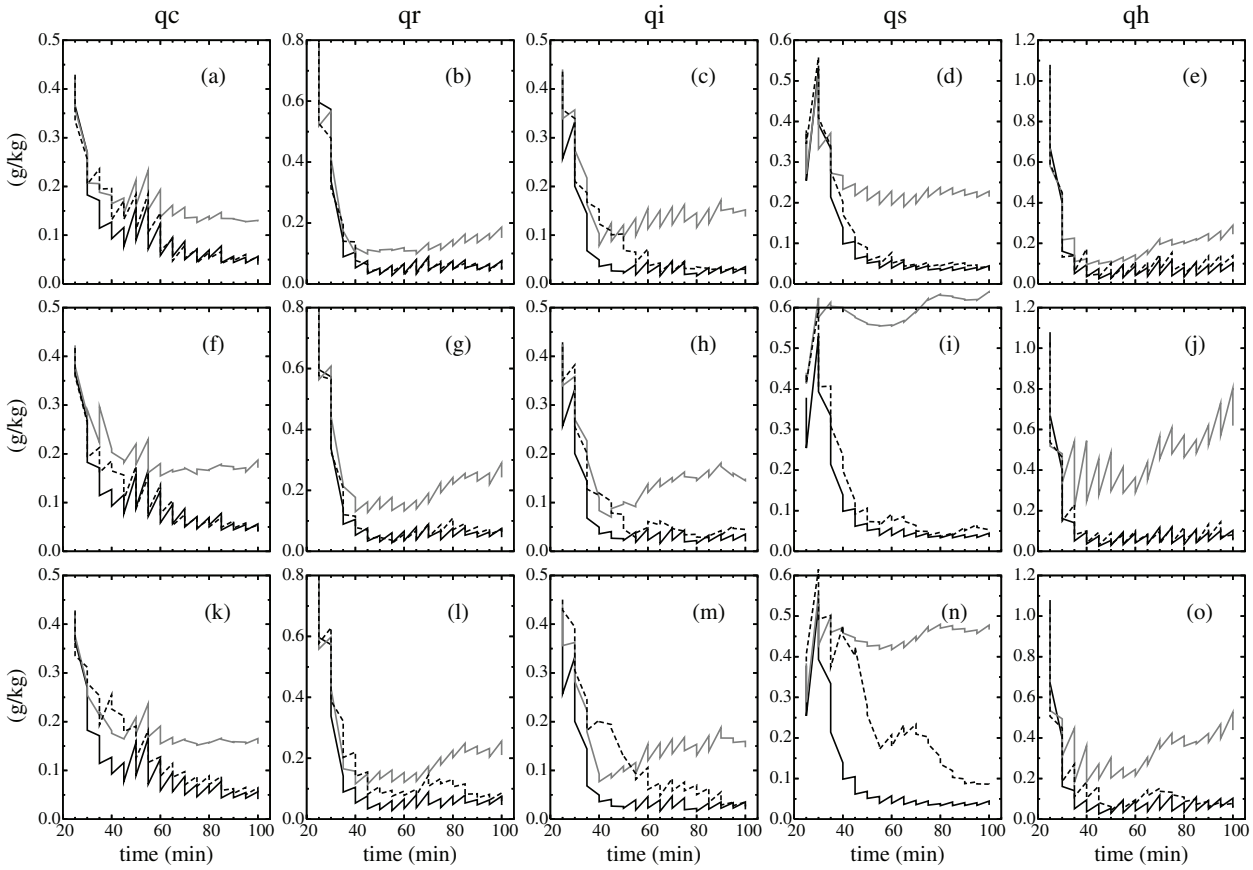

Fig. 10. As Fig. 3 but for three four-parameter (n_{0r}, n_{0s}, n_{0h}, ρ_h) estimation experiments, starting from initial guesses of (n_{0r}, n_{0s}, n_{0h}, ρ_h) = (0.2 m^{-4}, 0.3 m^{-4}, 0.004 m^{-4}, 700 kg m^{-3}) (first row); (n_{0r}, n_{0s}, n_{0h}, ρ_h) = (0.03 m^{-4}, 0.007 m^{-4}, 0.04 m^{-4}, 400 kg m^{-3}) (second row), and (n_{0r}, n_{0s}, n_{0h}, ρ_h) = (0.03 m^{-4}, 0.3 m^{-4}, 0.04 m^{-4}, 700 kg m^{-3}) (third row), which correspond to the black curves in the 1st, 2nd and 3rd column of Fig. 9, respectively. To be consistent, 100 ensemble members are used in the control experiment shown here.

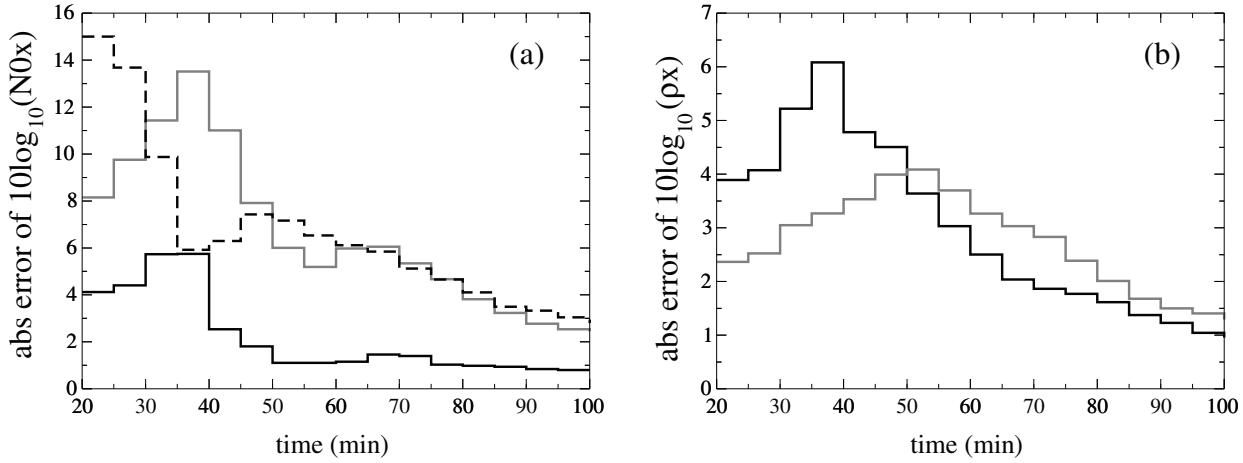

Fig. 11. The evolution of average ensemble-mean absolute errors of (a) $10\log_{10}(n_{0r})$ (solid black), $10\log_{10}(n_{0s})$ (solid gray), $10\log_{10}(n_{0h})$ (black dashed), and (b) $10\log_{10}(\rho_h)$ (solid gray) and $10\log_{10}(\rho_s)$ (solid black), calculated from 32 experiments starting from different initial guesses that simultaneously estimate (n_{0r}, n_{0s}, n_{0h}, ρ_h, ρ_s) using 100 ensemble members.

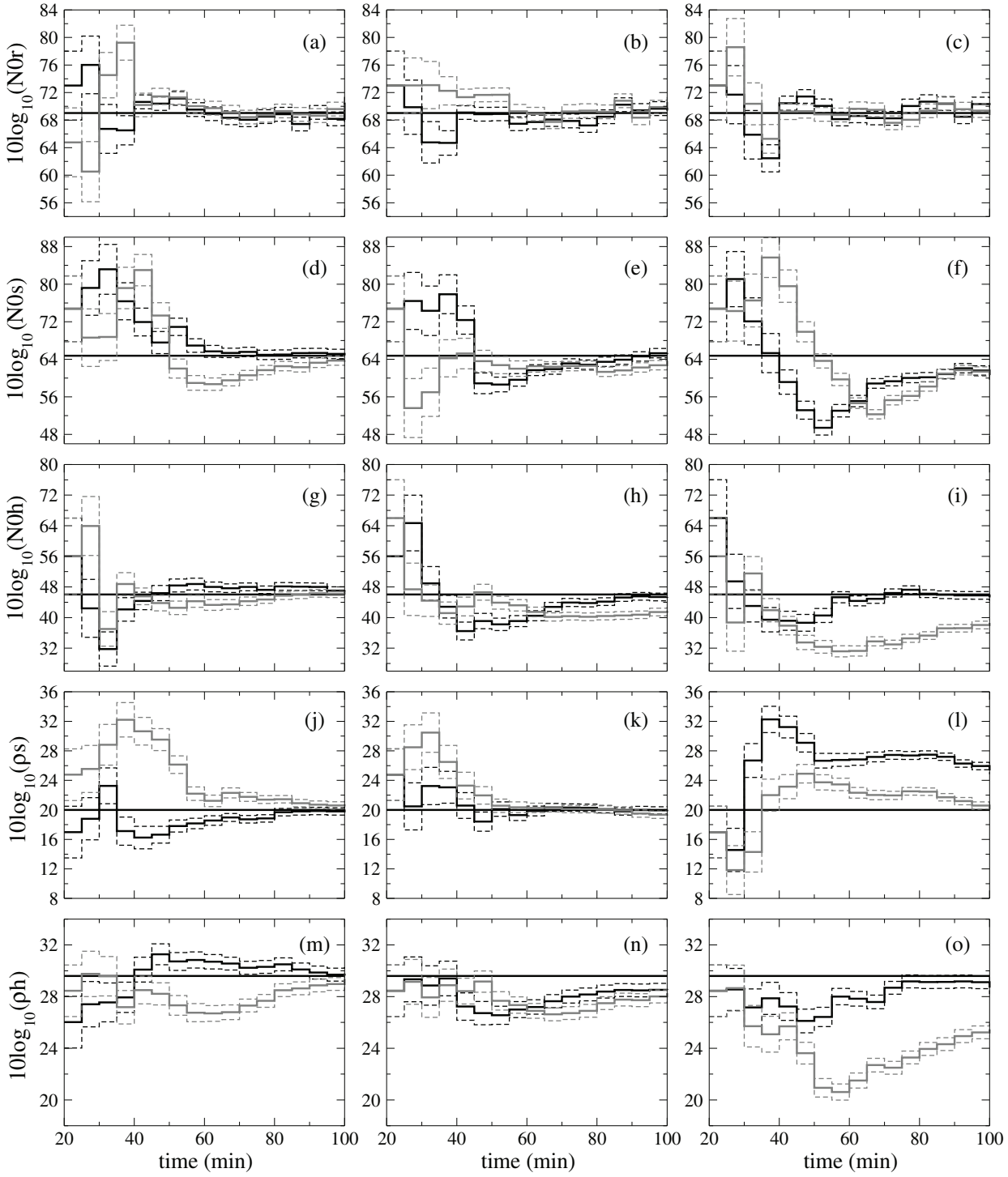

Fig. 12. As Fig. 4 but for experiments estimating five parameters simultaneously, using 100 ensemble members. Parameters shown are for n_{0r} (a)-(c), n_{0s} (d)-(f), n_{0h} (g)-(i), ρ_s (j)-(l), and ρ_h (m)-(o). The results of 6 of a total of 32 experiments with different initial guesses of $(n_{0r},\ n_{0s},\ n_{0h},\ \rho_h,\ \rho_s)$ are presented (2 in each column), with each experiment represented by the same gray level of curves in each column.

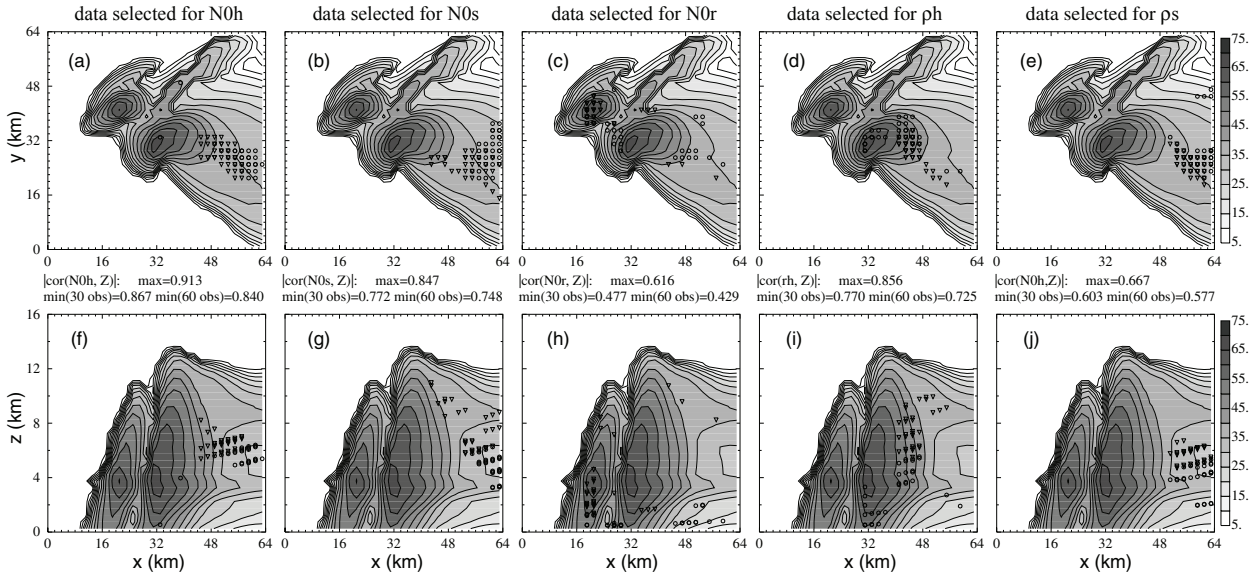

Fig. 13. The circles and triangles indicate the locations of the reflectivity data that were used in the single-parameter estimation experiments, which correspond to (b), (e), (i), (l) and (m) in Fig. 1. The data points are projected to the horizontal *x*-*y* (first row) and *x*-*z* vertical (second row) planes. The circles represent the data points when 30 data are used for parameter estimation. The triangles represent the additional 30 data points when 60 data are used. The shading and thin solid contours represent composite or column maximum reflectivity of the truth simulation in *z* (a-e) and *y* (f-j) directions. The maximum and minimum values of the correlation coefficient at those data points are indicated by the plots.

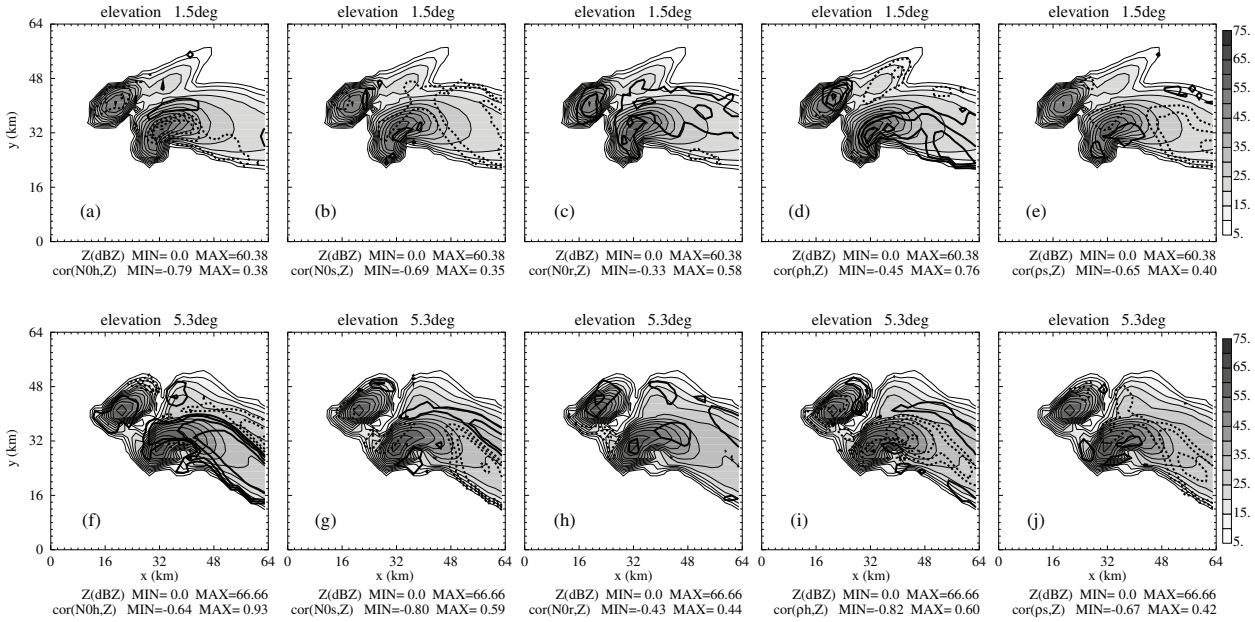

Fig. 14. Correlation coefficients calculated from the forecast ensemble at $t = 70$ min from single-parameter estimation experiments. The correlation coefficients [thick solid (dashed) contours represent positive (negative) values at intervals of 0.2] between Z at the 1.5° radar elevation and n_{0h} (a), n_{0s} (b), n_{0r} (c), ρ_h (d), and ρ_s (e); and the correlation coefficients between Z at 5.3° elevation and n_{0h} (f), n_{0s} (g), n_{0r} (h), ρ_h (i), and ρ_s (j). The shading with thin solid contours shows the Z fields from the truth simulation.

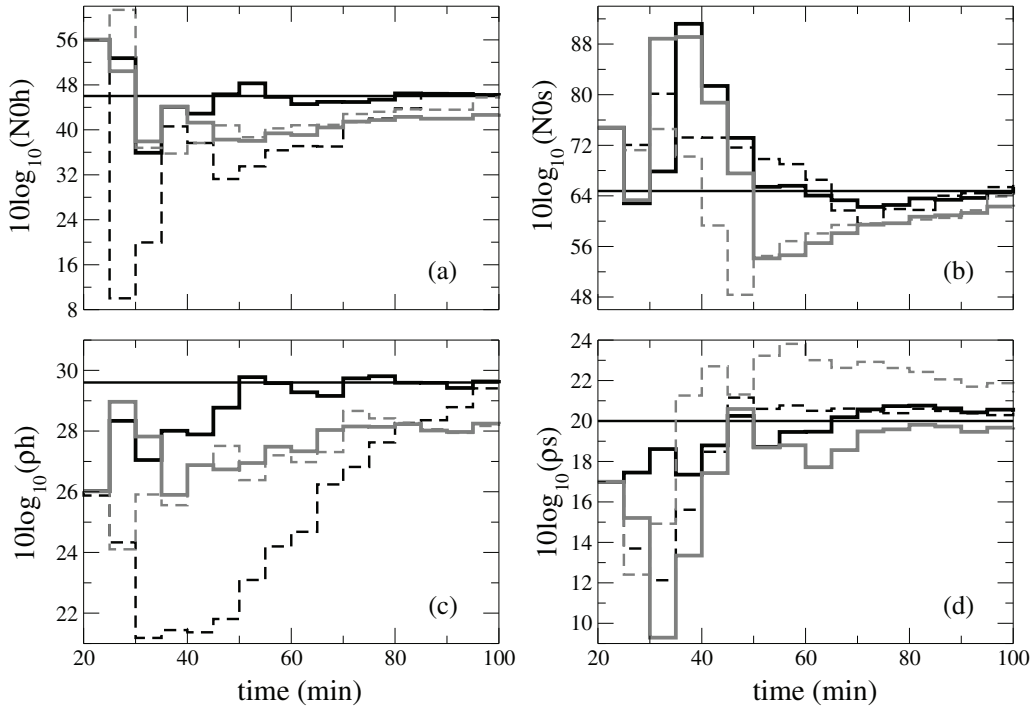

Fig. 15. The evolutions of the ensemble means together with the true values (straight lines) of $10\log_{10}(n_{0h})$ (a), $10\log_{10}(n_{0s})$ (b), $10\log_{10}(\rho_h)$ (c) and $10\log_{10}(\rho_s)$ (d), from experiments estimating (n_{0r}, n_{0s}, n_{0h}, ρ_s, ρ_h) starting from (4×10^5 m^{-4}, 3×10^7 m^{-4}, 3×10^7 m^{-4}, 50 kg m^{-3}, 400 kg m^{-3}). The different line types in each panel represent experiments using different realizations of the initial parameter ensemble.

Table 1. List of the true value of each microphysical parameter and the true value P_i^t , the upper bound $\overline{P}_i$ and lower bound $\underline{P}_i$ of each logarithmically transformed microphysical parameter $P_i = 10\log_{10}(p_i)$. σ_{P_i} stands for the standard deviation of the initial parameter perturbations for P_i , and $\underline{\sigma}_{P_i}$ is minimum ensemble spread of P_i used in ensemble inflation.

Parameter p_i/P_i	p_i^t	P_i^t	$\underline{P}_i$	$\overline{P}_i$	σ_{P_i}	$\underline{\sigma}_{P_i}$
n_{0h} (m^{-4})/10log$_{10}$(n_{0h})	4×10^4	46.02	26.02	66.02	10	1.0
n_{0s} (m^{-4})/10log$_{10}$(n_{0s})	3×10^6	64.77	56.9897	80	7	1.0
n_{0r} (m^{-4})/10log$_{10}$(n_{0r})	8×10^6	69.03	64.77	79.03	5	1.0
ρ_h (kg m^{-3})/10log10(ρ_h)	913	29.6	26.02	29.6	2	0.5
ρ_s (kg m^{-3})/10log10(ρ_s)	100	20.0	13.01	26.02	3.5	0.5

Table 2. The three initial guesses for each parameter in its original form p_0^m and the logarithmical form P_0^m ($m = 1, 2, 3$), which are used in single-parameter estimation experiments.

Parameter p_i	p_0^1	P_0^1	p_0^2	P_0^2	p_0^3	P_0^3
n_{0h} (m^{-4})	4×10^3	36.02	4×10^5	56.02	4×10^6	66.02
n_{0s} (m^{-4})	7×10^5	58.45	3×10^7	74.77	1×10^8	80
n_{0r} (m^{-4})	3×10^6	64.77	2×10^7	73.01	8×10^7	79.03
ρ_h (kg m^{-3})	400	26.02	700	28.45	750	28.75
ρ_s (kg m^{-3})	50	16.99	300	24.77	400	26.02

Table 3. Two initial guesses of each parameter in the original form p_0^m and the logarithmical form P_0^m ($m = 1, 2$) used in multiple-parameter estimation experiments.

Parameter p_i	p_0^1	P_0^1	p_0^2	P_0^2
n_{0h} (m^{-4})	4×10^5	56.02	4×10^6	66.02
n_{0s} (m^{-4})	7×10^5	58.45	3×10^7	74.77
n_{0r} (m^{-4})	3×10^6	64.77	2×10^7	73.01
ρ_h (kg m^{-3})	400	26.02	700	28.45
ρ_s (kg m^{-3})	50	16.99	300	24.77